

Study of Ferrocene Dicarboxylic Acid on Substrates of Varying Chemical Activity

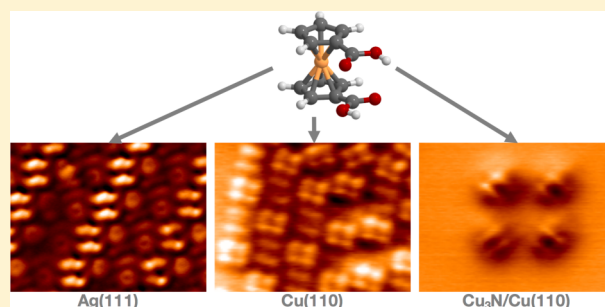
J. Berger,^{*,†} K. Kořmider,[†] O. Stetsovych,[†] M. Vondráček,[‡] P. Hapala,[†] E. J. Spadafora,[†] M. Švec,[†] and P. Jelínek^{*,†}

[†]Institute of Physics, Academy of Sciences of the Czech Republic, Cukrovarnická 10, CZ-16200 Prague, Czech Republic

[‡]Institute of Physics, Academy of Sciences of the Czech Republic, Na Slovance 1999/2, CZ-18221 Prague, Czech Republic

S Supporting Information

ABSTRACT: Ferrocene-based molecules are extremely appealing as they offer a prospect of having built-in spin or charge functionality. However, there are only limited number of studies of structural and electronic properties on surfaces so far. We investigated the self-assembly processes of 1,1'-ferrocene dicarboxylic acid molecules ($C_{12}H_{10}FeO_4$) on both metallic (Ag(111), Au(111), and Cu(110)) and insulating ($Cu_3N/Cu(110)$) surfaces with high-resolution ncAFM/STM, XPS, and NEXAFS. The experimental evidence is corroborated with total energy DFT calculations and ncAFM simulations. The combined experimental and theoretical analysis allows detailed understanding of the unique arrangement and adsorption geometries of the molecules on different substrates, as well as the different chemical stability of the carboxylic (COOH) groups. The molecules on noble (Ag, Au) surfaces show only a weak interaction with the substrate forming a complex self-assembled pattern, driven by weak intermolecular interactions. In contrast, the analysis reveals the carboxylic groups undergo dehydrogenation on the Cu(110) and $Cu_3N/Cu(110)$. As a result, the oxygen atoms form strong chemical bonds to the substrate Cu atoms and impose an orientation on the ferrocene cyclopentadienyl rings perpendicular to the substrate.



Metallocenes $M(C_5H_5)_2$, the molecules composed of two planar cyclopentadienyl anions (C_5H_5) with a metal (M) atom in between, have received attention over the past three decades mainly as catalysts and building blocks of organometallic polymers. Nowadays, due to the increasing capabilities of solid surface control methods and the development of molecular electronics they are considered as promising candidates of basic operational unit for future nanodevices. For example, the ferrocene $Fe(C_5H_5)_2$ molecule undergoes a one-electron oxidation at low potential. This property makes it a suitable candidate for building blocks of molecular quantum cellular automata.^{1–4} In such devices, a couple of ferrocene (Fc) molecules (or its derivatives) would act as a couple of quantum wells for a charge moving between them.

Efficient and reproducible fabrication of desired structures on surfaces is a first step toward realization of such devices. Molecular self-assembly at solid substrates proved to be an efficient method of obtaining nanostructures of the required characteristics. To self-assemble the Fc molecules, proper understanding of their electronic properties,⁵ intermolecular interactions, as well as their interaction with substrate^{6–10} is essential.

Self-organization of molecular systems can be strongly influenced by functional groups that modify the binding behavior of molecules.^{11–14} For example, a proper functionalization can determine the dimensionality of a self-assembly.^{15,16}

Hydrogen bonds O–HO between two carboxylic groups (COOH) groups can be classified as intermediately strong¹⁷ with a bonding angle of 180° . Thus, they can serve as very powerful noncovalent connectors for supramolecular networks.^{15,18}

On the other hand, carboxylic acids are biologically important compounds in living systems. For example, fatty acid esters are important components of many cell membranes, proteins are polymers of amino acids, and many compounds in intermediary metabolism are carboxylic acids.¹⁹ So it is desirable to study their chemical stability in the presence of different metals.

In this work, we study behavior of the 1,1'-ferrocene dicarboxylic acid molecules (FcDA, see Figure 1a) on different metals (Ag(111), Au(111), and Cu(110)) and on insulating ($Cu_3N/Cu(110)$) substrate. We performed complex experimental characterization of these systems, using high-resolution noncontact atomic force microscopy/scanning tunneling microscopy (ncAFM/STM) with functionalized tips and X-ray photoemission/near-edge X-ray absorption fine structure (XPS/NEXAFS) measurements. We also carried out the total

Received: June 14, 2016

Revised: August 19, 2016

Published: August 22, 2016



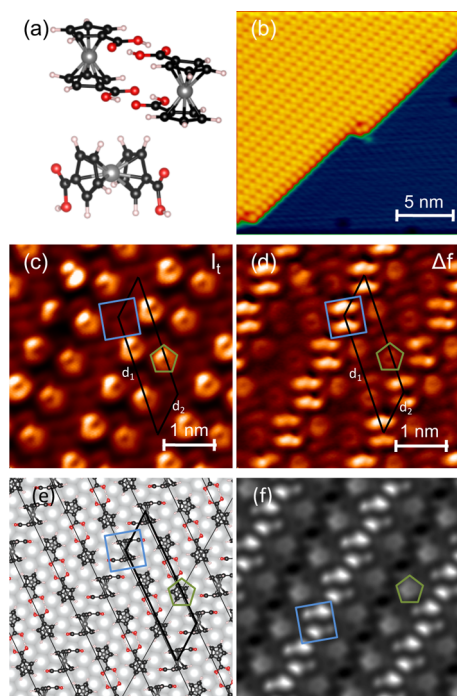


Figure 1. Periodic structure of FcDA molecules adsorbed on Ag(111) substrate: (a) ball-and-stick model of main building blocks (FcDA upstanding dimer and lying monomer) of the structure. H, O, C, and F atoms are marked by white, red, dark gray, and light gray colors, respectively. (b) STM image ($20 \times 20 \text{ nm}^2$) of a FcDA molecular island on Ag(111) ($U = 0.5 \text{ V}$, $I_t = 20 \text{ pA}$). (c,d) STM tunneling (I_t) and AFM frequency shift (Δf) images recorded with a CO-functionalized tip in a constant-height mode over a small portion ($5 \times 5 \text{ nm}^2$) of the island ($U = -10 \text{ mV}$). Black rhomboid represents the unit cell, $d_1 = 2.4 \text{ nm}$, $d_2 = 0.9 \text{ nm}$, and the angle between d_1 and d_2 is 45° . (e,f) simulated model of FcDA periodic structure from panels (c,d) with simulation of its nAFM image^{21,22} (for more details see Supporting Information Figure S3i).

energy density functional theory (DFT) calculations and AFM simulations to rationalize the experimental evidence.

The paper is organized as follows. First, we will present the experimental results of FcDA on Ag(111) and Au(111) surface followed by the related theoretical calculations. Second, we will summarize the experimental and theoretical results of FcDA on Cu(110) and on the insulating $\text{Cu}_3\text{N}/\text{Cu}(110)$ substrate. Next, we will discuss the obtained results to understand the unique behavior of FcDA on each investigated surface.

Results. FcDA on Ag(111) and Au(111). *STM/nAFM Experiment.* Deposition of the FcDA molecules onto a clean Ag(111) surface at room temperature (see Figure 1b), lasting 2 min resulted in a submonolayer coverage of the substrate. The molecules formed compact and stable islands that can be visualized in the STM topography images even at room temperature. Figure 1b shows an edge of a representative FcDA island on the Ag(111) acquired at 1.2 K. An almost perfect order is observed at the whole extent of the islands. The metallic tip barely allows localizing the individual molecules that appear to form aligned directional stripes within the islands. We observed very similar behavior of FcDA molecules deposited on Au(111) surface at room temperature (see STM images acquired at room temperature Supporting Information Figure S1).

A common method of improving AFM/STM resolution is to functionalize the tip with CO molecule, according to well-

known schemes.²⁰ With such tip, we examined the arrangement and orientation of the molecules in a great detail. Figure 1c,d shows maps of simultaneously taken tunneling current and frequency shift with the CO-decorated tip scanning in the constant height above sample. Both maps reveal a complex but regular structure consisting of multiple pairs of pentagons arranged in rows, mutually interconnected by linear double lobes. Although the contrast of these features varies between the channels, both represent the same elementary pattern. The pentagons and the linear double lobe motives have a size comparable to the diameter of individual FcDA molecules, that is, $\sim 3 \text{ \AA}$. Their size and appearance suggest a presence of the FcDA molecules in at least two orientations on the substrate: the pentagons mark the molecules with cyclopentadienyl rings parallel to the substrate (standing-up) and the double linear lobes the molecules with their rings perpendicular (laying-down). Figure S2 in Supporting Information presents a series of high-resolution images at the different tip–sample distances taken with CO molecule decorated tip. Similar STM contrast and its interpretation as the two different Fc molecule orientations on Cu(111) and Cu(100) surfaces have been described previously.⁷

XPS and NEXAFS. The STM/nAFM images provide information on the sub monolayer growth and orientation of FcDA on the investigated substrates. However, they cannot access the information about a molecule–substrate interface. Because the FcDA molecule at the metallic substrate in principle may be adsorbed by two COOH groups, information about changes in chemical composition of these groups is important for a proper interpretation of the observed molecular structure. Dehydrogenation, the simplest chemical modification of these groups, can be monitored by observation of O 1s core level line shape in the XPS spectra. In this particular case as the COOH group includes two inequivalent oxygen atoms, two different O 1s peaks corresponding to carbonyl (CO) and hydroxyl (OH) are expected in the XPS spectrum. In the case of a dehydrogenated group (COO^-), however, all O 1s levels are degenerate and therefore would produce only single spectral line.

Figure 2a shows XPS measurement of O 1s levels for the FcDA molecules on the Ag(111) substrate. The line shape is very broad with a notable dip in the center. A fit shows two components of equal shape at 532.0 and 534.5 eV, indicating equal number of hydroxyl and carbonyl groups. This corresponds to a presence of the unaltered COOH groups.

Additionally, to extract information about the orientation of the FcDA molecule with respect to the substrate, we measured the NEXAFS K-edge profiles of C atoms. Figure 2b (blue color) shows a prominent set of π -resonances in the grazing incidence geometry and a strong σ signature in the normal incidence geometry. Because the molecules have a π -system on the cyclopentadienyl rings, we can attribute these features to a prevailing orientation of the rings parallel to the substrate, that is, the upstanding configuration of the molecules.

DFT/nAFM Simulation. Next, we carried out the total energy DFT calculations and AFM simulations to rationalize the experimental data. Keeping in mind the periodicity of the STM and nAFM patterns together with the assumption of preserving chemical integrity of the COOH groups, we analyzed several possible geometrical arrangements of the FcDA molecules on the Ag(111) surface (see Supporting Information Figure S3). We should stress that the self-assembled FcDA monolayer is incommensurate with Ag(111)

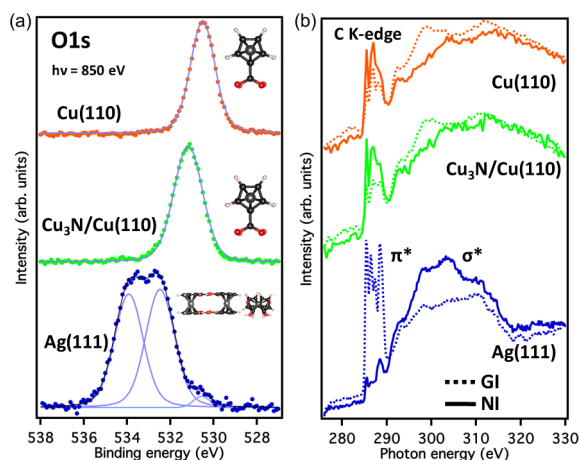


Figure 2. Analysis of selected electronic states of FcDA molecules adsorbed Cu(110), Cu₃N/Cu(110), and Ag(111) substrate: (a) XPS spectra (dots) of O 1s of FcDA molecule on different substrates adsorbed on different substrates (fits marked by solid lines). The inset models schematically indicate the positions of the molecules with respect to each substrate. (b) NEXAFS spectra of the C K-edge corresponding to the samples with the spectra in (a). The solid lines represent normal incidence (NI) and dotted lines the grazing incidence (GI) geometries.

surface. Therefore, we had to modify slightly ($\sim 5\%$) the lattice constant of Ag(111) surface to make the calculations feasible. As a selective criteria we chose averaged binding energy $\langle E_b \rangle$ (for its definition see Supporting Information eq 1) and a simulation-to-experiment match of an ncAFM image.

The lowest adsorption energy per molecule $\langle E_b \rangle$ (Supporting Information Table S1) is achieved for a structure consisting of a periodic mixture of FcDA upstanding dimers (pentagons in Figure 1c,d) and lying monomers (squares in Figure 1c,d), very similar to the experimental observation. Moreover, comparing all calculated ncAFM images it is evident (see Supporting Information Figure S3) that only this ordering gives the overall agreement with the experimental images (see Figure 1d,f). We should note that we found two energetically very similar structures that differ just by switching of position of hydrogen atom on one of the carboxylic groups on FcDA, see Supplementary Figure S3e,h). We cannot distinguish either from the total energies obtained by DFT or AFM simulations between the two structures and if it is even possible that they coexist. The perfect agreement between experimental and theoretical ncAFM images was achieved by a small elevation (0.8 Å) of the lying monomers outward from the surface (Supporting Information Figure S3i). We can attribute this small inconsistency to either the enforced commensurability of the molecular layer with the substrate, or an improper description of exchange-correlation energy (PBE functional), or to inaccurate description of VdW interaction. Finally, this effect could be also caused by bending of the molecules on surface during scanning process, which is not considered in our AFM simulation model.

To understand the driving mechanism behind the self-assemble process, we also analyzed the strength of different intermolecular as well as molecule–substrate interactions involved in the process (see Figure 3). The results show that a hydrogen bonding between the opposite carboxyl groups is the strongest one ($\Delta E_{\text{tot}} \sim 0.75$ eV per group). Interaction of molecules with a substrate (MS_1 , MS_2 , DS) is a bit weaker

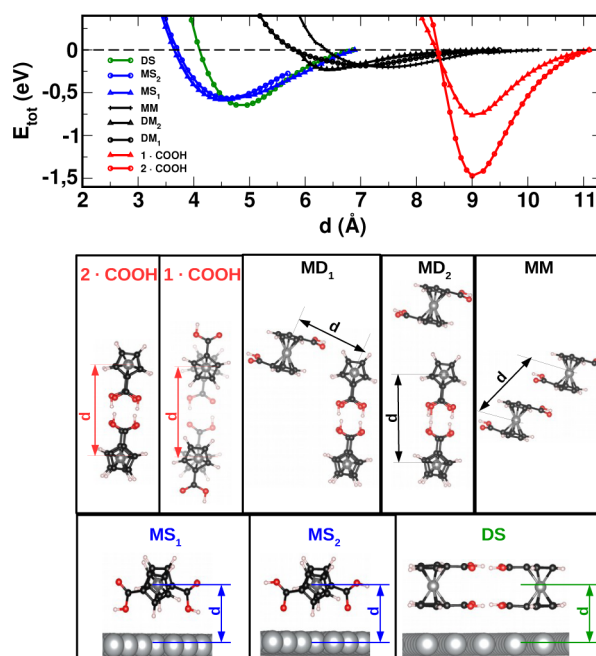


Figure 3. Interactions of separated components of the most stable periodic structure of FcDA molecules at the Ag(111) substrate (Supplementary Figure S3h). The DFT total energy calculations of isolated subsystems was done for an increasing distance d and fixed geometry of the molecules. The strongest interaction can be observed between two molecules forming a dimer (2-COOH) in which two pairs of the COOH groups form well-defined hydrogen bonds. Interaction of only one such a pair is comparable with the dimer–substrate (DS) and the monomer–substrate (MS_1 , MS_2) interactions and is more than twice stronger than the monomer–dimer (DM_1 , DM_2) and the monomer–monomer (MM) interactions.

($\Delta E_{\text{tot}} \sim 0.6$ eV per molecule) and does not depend on a molecule orientation. The DFT calculations reveal only negligible charge transfer between FcDA molecules and Ag substrate. Thus, the interaction between FcDA molecules and the substrate is mostly driven by the vdW interaction. The weakest are the upstanding dimer–lying monomer and lying monomer–lying monomer vdW interactions ($\Delta E_{\text{tot}} \sim 0.2$ eV). However, they occur frequently in the optimal arrangement, which in sum can form net interaction comparable to the electrostatic interaction between the carboxylic groups. Thus, they also play important role in the final molecular arrangement on the Ag surface. We believe that the peculiar arrangement of FcDA molecules on Ag(111) surface, including FcDA molecules in parallel and perpendicular orientation with respect to substrate, is the result of complex interplay between the presented electrostatic and vdW interactions.

FcDA on Cu(110) and on Cu₃N/Cu(110). STM/ncAFM Experiment. We also deposited the FcDA molecules on the Cu(110) surface partially covered by insulating Cu₃N adlayer. Figure 4 shows a STM topography image of a border between the Cu₃N/Cu(110) island (left part of Figure 4) and clean Cu(110) (right part of Figure 4). Different adsorption configuration of the FcDA molecules at these two regions are clearly visible. On the clean Cu(110) surface, the molecules aggregate next to the atomic step or make compact islands, while on the Cu₃N adlayer they form small loose clusters sparsely distributed over the whole area.

A detailed image of the interior of the FcDA island on Cu(110) aggregate (Figure 5b) shows rectangular features.

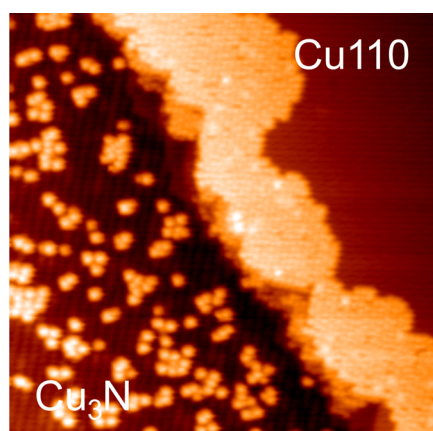


Figure 4. STM image ($50 \times 50 \text{ nm}^2$) of the FcDA molecules adsorbed along a step edge of Cu_3N adlayer on $\text{Cu}(110)$ surface. The $\text{Cu}_3\text{N}/\text{Cu}(110)$ substrate is covered by distributed FcDA molecules, whereas on $\text{Cu}(110)$ they agglomerate along a step edge. Image is taken with metallic tip and with following scanning conditions: $U = 0.5 \text{ V}$, $I_t = 20 \text{ pA}$.

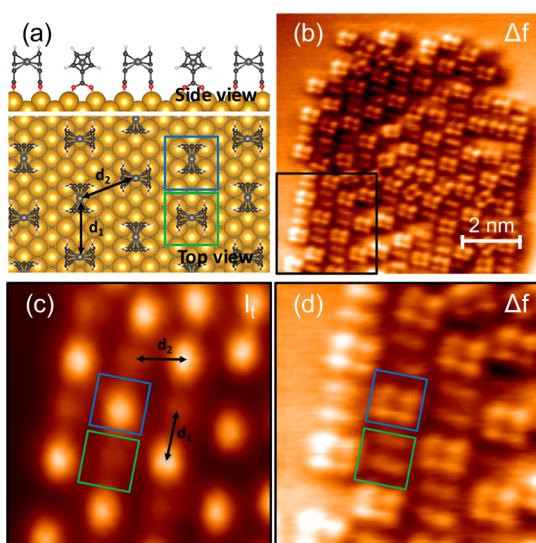


Figure 5. An island of FcDA molecules on $\text{Cu}(110)$ substrate: (a) Ball-and-stick model of the FcDA molecules adsorbed on $\text{Cu}(110)$. Top part shows a side view on substrate with FcDA molecules in standing up position. Lower part shows top view in FcDA adsorbed on $\text{Cu}(110)$ substrate ($d_1 = 7.65 \text{ \AA}$, $d_2 = 7.68 \text{ \AA}$); (b) nCAFM constant height image ($10 \times 10 \text{ nm}^2$, $U = 10 \text{ mV}$); (c–d) Simultaneously taken tunneling (I_t) frequency shift (Δf) images of the region marked in the panel (b). Alternating chessboard-like contrast is clearly visible in both figures. Green and blue squares denote corresponding molecules. Arrows labeled d_1 and d_2 denotes intermolecular distances (experimentally measured) corresponding to (a), $d_1 = 7.3 \text{ \AA}$ and $d_2 = 7.9 \text{ \AA}$.

Their order is short-range with some features rotated with respect to the majority of the others by roughly $\pm 45^\circ$. Alternating contrast, either with four round lobes or two stripes (in Δf channel, Figure 5b,d), is similar to the contrast of the FcDA monomers on $\text{Ag}(111)$. Therefore, we associate them with the cyclopentadienyl of individual FcDA molecules pointing the carboxylic groups perpendicular to the substrate. A detailed inspection of the island (Figure 5c,d) shows that both STM tunneling current as well as AFM frequency shift

measurements present an alternating contrast (chessboard-like pattern). We discuss the origin of this contrast later.

A closer look at the FcDA on the $\text{Cu}_3\text{N}/\text{Cu}(110)$ (Figure 6a–c) shows distributed molecules with a similar contrast

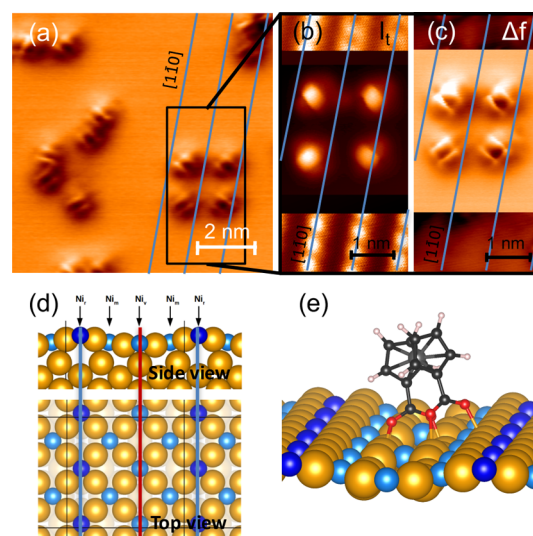


Figure 6. FcDA molecules adsorbed on $\text{Cu}_3\text{N}/\text{Cu}(110)$ substrate: (a) Frequency shift constant height image, $10 \times 10 \text{ nm}^2$, $U = 10 \text{ mV}$. Blue lines denote $[1\bar{1}0]$ nitrogen rows. (b) Detailed tunneling current and (c) frequency shift images of four molecules in (a), $3.5 \times 7.0 \text{ nm}^2$, $U = 1 \text{ mV}$. Nitrogen rows are marked by blue lines. To obtain resolution on both the $\text{Cu}_3\text{N}/\text{Cu}(110)$ and FcDA, the tip was retracted by 0.54 nm in the middle part of the scan (region of four FcDA molecules). (d) Ball-and-stick model of $\text{Cu}_3\text{N}/\text{Cu}(110)$. Rows of nitrogen atoms are dark blue, denoted by blue line. Valley between these rows consists of three rows of nitrogen atoms (light blue), denoted by red line. (e) Model of the FcDA, bonded in standing up configuration, perpendicular to the $\text{Cu}_3\text{N}/\text{Cu}(110)$ surface.

(Figure 6a) as on the $\text{Cu}(110)$, suggesting a comparable adsorption mechanism. Adsorption on this surface is, however, more complicated due to complex structure of the substrate.^{23,24} Corrugation of the Cu_3N adlayer on the $\text{Cu}(110)$ result in characteristic nitrogen ridges separated by the valleys, both oriented along the $[1\bar{1}0]$ direction. Figure 6d shows the ball-and-stick model of Cu_3N adlayer on the $\text{Cu}(110)$. The dark and light blue spheres represent the N lines. The dark blue spheres (marked with blue line) represent the toppest row of N atoms, that creates the ridges in STM image (see Figure 6b). Light blue spheres represent N atoms that create the N rows in the valleys. The lowest N row is labeled by red line.

Detailed inspection of the Cu_3N area in Figure 6a resolves the $[1\bar{1}0]$ nitrogen ridges, which allows us to determine adsorption position of the FcDA on the surface Figure 6b. We found that about $\sim 80\%$ of molecules adsorb at the valleys and only $\sim 20\%$ are located at the ridges (see Supporting Information Figure S4a–d). Careful analysis of an overlay of nitrogen ridges over the FcDA nCAFM images shows (Figure 6b,c) that adsorption takes place at the sides of the valleys rather than in their centers. Moreover, it is evident that most of the molecules are oriented $\pm 45^\circ$ with respect to the $[1\bar{1}0]$ rows.

XPS and NEXAFS. The XPS spectra were measured for a separately prepared $\text{Cu}(110)$ and the full adlayer of $\text{Cu}_3\text{N}/\text{Cu}(110)$ substrates. The coverage of the substrate by the FcDA

was kept below 1/4 monolayer. In both experiments, a single O 1s spectral peak (530.2 eV on Cu(110), and 530.5 eV on Cu₃N/Cu(110)) appeared immediately after the deposition of the FcDA (Figure 2a), indicating a full dehydrogenation of the COOH groups of FcDA molecules. This effect has been already reported for reaction of formic acid (HCOOH) with Cu(110).^{25,26}

The NEXAFS C K-edge profiles of the FcDA at Cu(110) and Cu₃N/Cu(110) substrates (Figure 2b) suggest a prevailing orientation of the π -system (cyclopentadienyl rings) perpendicular to the substrate (laying-down configuration),

DFT/ncAFM Simulation. To get more insight into the experimental observations, we performed the total energy DFT calculations of different arrangements of FcDA molecules on both Cu(110) and Cu₃N/Cu(110) substrates. On the basis of the XPS and NEXAFS measurements as well as the previous reports of a dehydrogenation of HCOOH at Cu(110),²⁷ we concentrated on an adsorption of dehydrogenated FcDA molecules.

In the case of the Cu(110) surface, following the experimental evidence, we tested different structures of FcDA molecules aligned along the $[1\bar{1}0]$ substrate rows. We found that the molecule interacts strongly with the substrate (the binding energy $E_b = -8.53$ eV) through O–Cu bonds ($d_{\text{O–Cu}} = 1.95$ Å) with COO groups oriented along the $[1\bar{1}0]$ rows (Supporting Information Figure S5b). More importantly, both oxygen atoms bind to the substrate in very similar way and the calculated O 1s levels of the dehydrogenated FcDA molecule on Cu(110) substrate confirms existence of only one XPS O 1s component. This indicates that FcDA molecules bind to the Cu(110) substrate via both COO groups (with four O–Cu bonds). To better understand an adsorption mechanism, we performed simulations of several FcDA arrangements. DFT total energy analysis shows that an alignment of cyclopentadienyl rings (as well as COO groups) along the $[1\bar{1}0]$ rows (Supporting Information Figure S5b) gives the most stable configuration ($E_b = -8.53$ eV). However, such an alignment locates all molecules in the same height, and such structure does not correspond to the chessboard pattern observed in the ncAFM/STM measurements, which indicate an alternating height of the molecules. The height of molecule above the surface can be altered by rotation of 90° around z-axis (Supporting Information Figure S5c), resulting in only a bit less stable structure ($E_b = -8.43$ eV). Additionally, the experimentally observed nonorthogonal structure (see Figure 5d) can be obtained by a translation of every second molecular row in the $[1\bar{1}0]$ direction (Supporting Information Figure S5d). This structure ($E_b = -8.43$ eV) gives distances between neighboring molecules $d_1 = 7.65$ Å and $d_2 = 7.68$ Å, see Figure 5a. That is in very good agreement with experimental evidence, $d_1 = 7.3$ Å and $d_2 = 7.9$ Å, see Figure 5c. The difference between theoretically calculated and experimentally measured values is below 10%.

In the case of the FcDA molecules on the Cu₃N/Cu(110) substrate, the situation is more complex. We carried out a series of total energy calculations considering different adsorption configurations of the dehydrogenated FcDA on the Cu₃N/Cu(110) substrate, including the surface with a N vacancy. All the optimized geometries can be found on Supporting Information Figure S6. We will analyze the adsorption mechanism in more details in the Discussion.

Discussion. The ncAFM/STM measurements show that self-assembled well-ordered periodic structure is created only at

the Ag(111) and Au(111) surface. On the contrary, on the Cu(110) surface, FcDA molecules tend to arrange in compact islands with a certain internal disorder. On Cu₃N/Cu(110) surface, FcDA molecules appear as randomly distributed in small clusters. Such a different behavior can be understood in terms of the possible dehydrogenation process on Cu-based surfaces, thus varying the strength of the molecule–surface and molecule–molecule interactions.

Namely, the presence of two peaks in the XPS O 1s levels spectra of FcDA at Ag(111) prove that adsorption at this substrate takes place without the COOH dehydrogenation. This observation is in line with a previous study, which reported that the formic acid (HCOOH) dehydrogenation at the same substrate is energetically unfavorable.²⁷ This observation is also confirmed by the very good agreement between the experimental and simulated ncAFM images, performed for the model with complete COOH groups, see Figure 1d,f. Moreover, theoretical analysis of an intermolecular and molecule–substrate interaction in this model reveals that the strength of molecule–substrate interaction is comparable with a binding of a pair of COOH groups. Thus, FcDA molecules create islands consisting of combination of pair of molecules bonded via COOH groups and single FcDA molecules that make rows between these pairs.

In the case of the Cu(110) surface, the dehydrogenation process on the carboxylic groups takes place, according to the presence of only one O 1s level peak in XPS spectra of FcDA on the Cu(110), see Figure 2a. Moreover, the total energy DFT calculations show that open shell COO[−] group binds strongly to topmost Cu atoms with the Fc unit pointing out of surface, see Figure 5a. This configuration can explain naturally the molecular contrast observed in the ncAFM images. The characteristic four-lobes (or double-stripes) visible in the experimental nc-AFM images, see Figure 5b, can be then related to the uppermost hydrogen atoms of carbon rings of the molecule. This configuration of the FcDA is also supported by the NEXAFS measurements.

On the other hand, the internal order of islands of FcDA on the Cu(110) is more complex. Typically, the islands grow from step edges. They are relatively compact but with only local order, giving a hint on the driving forces of their formation. The strong bonding to the substrate is the major factor preventing a long-range order of the self-assembly, driven by the intermolecular attraction. Molecules within the islands absorb predominantly on top of the Cu rows forming chains along the $[1\bar{1}0]$ direction. Our total energy DFT simulations of different orientation of FcDA/Cu(110) with respect to the Cu $[1\bar{1}0]$ rows reveal very similar binding energies. The two periodic models consisting of two alternating FcDA configuration (Supplementary Figure S5) give very similar total energies, which can justify the coexistence of different local domains. From detailed inspection of the experimental STM/ncAFM images it is evident, that the domains are separated by FcDA molecules oriented 45° with respect the Cu $[1\bar{1}0]$ rows.

We can only speculate what is the formation mechanism of compact FcDA islands on the Cu(110). We can see the formation of the compact island as a chain process beginning at the Cu(110) step edges, where the adsorption of a single FcDA molecule is energetically favorable. The formation of the short-range ordered structure indicates that the adsorption of FcDA molecule enhances the possibility of the dehydrogenation of another FcDA molecule in its vicinity. A plausible scenario explaining this effect could be that the adsorption of FcDA

molecules induces a variation of electronic density near the Fermi level on adjacent Cu atoms, for example, shift of d-orbitals toward the Fermi level. This effect can enhance their reactivity and thus facilitates the dehydrogenation process with respect to the regular Cu surface atoms located far from the adsorbed FcDA molecules. Consequently the molecular chains along the Cu $[1\bar{1}0]$ rows are formed. However, very similar binding energies of the different adsorption configurations of FcDA molecule prevents the long-range order formation of well ordered structure.

On the $\text{Cu}_3\text{N}/\text{Cu}(110)$ substrate, the COOH dehydrogenation is also confirmed by the presence of the only one O 1s peak in XPS spectra, see Figure 2a. The standing up configuration of the dehydrogenated FcDA is also supported by NEXAFS spectra and the ncAFM images, which show very similar contrast as the one taken on the Cu(110) with two parallel lobes. However, the ncAFM images show that the FcDA molecules are oriented 45° with respect to the $[1\bar{1}0]$ rows. Nevertheless, our total energy DFT calculation of the various adsorption configurations at an ideal $\text{Cu}_3\text{N}/\text{Cu}(110)$ substrate reveal that it is not the most energetically favorable, see Supporting Information Table 2. The rotation of the FcDA molecule with respect to the $[1\bar{1}0]$ rows causes substantial mechanical strain because oxygen atoms cannot easily accommodate distances of the nearest Cu surface atoms underneath. The binding energy of the rotated configuration is about 1 eV higher with respect to the optimal structure, which is located on top of the $[1\bar{1}0]$ rows, see model F in Supporting Information Figure S6.

To understand this discrepancy between the experimental evidence and the theoretical calculations, we inspected additional possible adsorption geometries. We noticed that the $\text{Cu}_3\text{N}/\text{Cu}(110)$ phase contains substantial number of defects located in N-sites, most likely N-vacancies. Thus, we calculated several FcDA configurations with the N-vacancies, see Supporting Information Figure S6. The binding energy of these is more favorable comparing to those without vacancies, see Supporting Information Table 2. What is more, our DFT simulations reveal the optimal geometry of FcDA rotated 45° with respect to the $[1\bar{1}0]$ rows, which matches very well with the experimental ncAFM images, see ball-and-stick model of adsorbed FcDA in Figure 6e. Therefore, it is very likely that the FcDA adsorbs preferentially on Cu atoms near the N-vacancies. We should note the number of N-vacancies before the deposition of FcDA is in general higher than the number of the adsorbed FcDA molecules we found on the $\text{Cu}_3\text{N}/\text{Cu}(110)$ phase. Consequently, they can accommodate the amount of FcDA molecules on the $\text{Cu}_3\text{N}/\text{Cu}(110)$ phase observed in the experiment. On the other hand, we cannot rule out completely a scenario, where the FcDA molecule creates additional N-vacancies during the dehydrogenation process and forming ammonia that desorbs from the surface.

Summary. We performed a complex study of the adsorption of FcDA molecules on different (metallic and insulating) surfaces by means of ncAFM, STM, XPS, NEXAFS, and DFT calculations. We found very different behavior of FcDA molecules on noble metal (Ag, Au) and Cu-based surfaces. On the Ag(111) and Au(111) surfaces, the FcDA molecules interacts weakly with the substrate forming a complex self-assembled pattern. We were able to determine the molecular arrangement of the self-assembled molecular layer combining the high-resolution ncAFM images with CO-

decorated tip, total energy DFT calculation, and the simulation of ncAFM images.

In the case of Cu(110) and $\text{Cu}_3\text{N}/\text{Cu}(110)$ surfaces, FcDA molecules undergo a dehydrogenation of carboxylic groups. As a consequence, the FcDA are strongly bound to the substrate via oxygen atoms. On the Cu(110), the FcDA molecules tend to organize into relatively dense islands with internal disorder. The character of this structure reveals an surface-mediated attractive interaction between the molecules. On the other hand, we observe mostly random distribution of FcDA molecules on the $\text{Cu}_3\text{N}/\text{Cu}(110)$ surfaces. Our study indicates that the FcDA adsorption takes place most likely on Cu atoms residing near the native N-vacancies present in the $\text{Cu}_3\text{N}/\text{Cu}(110)$ layer. Thus, our study indicates that the Cu in general has critical influence on the stability of the carboxylic group.

Methods. The microscopy measurements were performed with a Joule-Thomson (JT) scanning probe microscope, manufactured by SPECS Surface Nano Analysis GmbH, in UHV conditions in the range of 10^{-10} mbar and at a temperature of 1.2 K. The imaging of the molecules was performed using a Kolibri sensor (also called needle-sensor) with a chemically etched tungsten tip. This setup allows for simultaneous measurement of the frequency shift (related to force) and tunneling current between an oscillating tip and the sample surface. The Kolibri sensor used during this experiment had a resonance frequency of 990 kHz with quality factor of 119 000 at 1.2 K and the stiffness 1080 kN/m. Upon insertion into UHV, the sensor tip was cleaned by Ar^+ sputtering. An oscillation amplitude of 50 pm was set for all the measurements in this work.

Spectroscopy measurements (XPS core levels and NEXAFS) were performed at the Elettra synchrotron, Italy on the Materials Science Beamline using SPECS Phoibos 150 electron analyzer. The samples used in this investigation were monocrystals of Au(111), Ag(111), and Cu(110). All samples were degassed in UHV at 550°C for 6 h and subsequently cleaned by cycles of Ar^+ ion sputtering and annealing to 550°C . The cleanliness of the surfaces was confirmed using low-energy electron diffraction (LEED).

The $\text{Cu}_3\text{N}/\text{Cu}(110)$ surface was prepared by 500 eV N_2^+ ion bombardment of the clean Cu(110) in 3×10^{-6} mbar of background N_2 and simultaneous annealing to 600°C . The duration of the procedure varied between 2 and 5 min, depending on the desired coverage.

FcDA molecules were thermally deposited from a quartz crucible directly on the sample held at room temperature. Temperature of the FcDA evaporation was 145°C . The pressure in the preparation chamber did not exceed 9×10^{-10} mbar.

We performed all the calculations with an ab initio method based on DFT. We used all-electron approach with numeric atom-centered orbital basis as implemented in the FHI-aims code.²⁸ We used the Perdew–Burke–Ernzerhof (PBE)²⁹ functional to account for the exchange-correlation energy, and the Tkatchenko–Scheffler method³⁰ to describe the dispersion energy. In each self-consistency step, we optimized electronic density so that changes in charge density ρ , sum of eigenvalues E_k , and total energy E_{tot} was smaller than 10^{-4} e, 10^{-2} eV, and 10^{-6} eV, respectively. For all structural relaxation, we used the Broyden–Fletcher–Goldfarb–Shanno optimization algorithm with a force convergence criterion equal 10^{-2} eV/Å. For the selected DFT-optimized atomic structures, we

simulated ncAFM images using the home-built simulation toolkit.^{21,22}

■ ASSOCIATED CONTENT

● Supporting Information

The Supporting Information is available free of charge on the ACS Publications website at DOI: 10.1021/acs.jpcc.6b05978.

FcDA molecules adsorption on Au(111), Ag(111), Cu(110), and Cu₃N/Cu(110) surfaces with corresponding calculated adsorption geometries (PDF)

■ AUTHOR INFORMATION

Corresponding Authors

*E-mail: bergerj@fzu.cz.

*E-mail: jelinekp@fzu.cz.

Notes

The authors declare no competing financial interest.

■ ACKNOWLEDGMENTS

We acknowledge the support by GACR, Grant 14-02079S and GACR Grant 14-374527G. X-ray spectroscopy experiments were supported by the Ministry of Education (LG15050 and LM2015088).

■ REFERENCES

- (1) Lu, Y.; Lent, C. S. A metric for characterizing the bistability of molecular quantum-dot cellular automata. *Nanotechnology* **2008**, *19*, 155703.
- (2) Lent, C. S.; Tougaw, P. D.; Porod, W.; Bernstein, G. H. Quantum cellular automata. *Nanotechnology* **1993**, *4*, 49.
- (3) Orlov, A. O.; Amlani, I.; Bernstein, G. H.; Lent, C. S.; Snider, G. L. Realization of a Functional Cell for Quantum-Dot Cellular Automata. *Science* **1997**, *277*, 928.
- (4) Amlani, I.; Orlov, A. O.; Toth, G.; Bernstein, G. H.; Lent, C. S.; Snider, G. L. Digital Logic Gate Using Quantum-Dot Cellular Automata. *Science* **1999**, *284*, 289–291.
- (5) García-Suárez, V. M.; Ferrer, J.; Lambert, C. J. Tuning the Electrical Conductivity of Nanotube-Encapsulated Metallocene Wires. *Phys. Rev. Lett.* **2006**, *96*, 106804.
- (6) Heinrich, B. W.; Limot, L.; Rastei, M. V.; Iacovita, C.; Bucher, J. P.; Djimbi, D. M.; Massobrio, C.; Boero, M. Dispersion and Localization of Electronic States at a Ferrocene/Cu(111) Interface. *Phys. Rev. Lett.* **2011**, *107*, 216801.
- (7) Ormaza, M.; Abufager, P.; Bachellier, N.; Robles, R.; Verot, M.; Bahers, T. L.; Bocquet, M.-L.; Lorente, N.; Limot, L. Assembly of Ferrocene Molecules on Metal Surfaces Revisited. *J. Phys. Chem. Lett.* **2015**, *6*, 395–400.
- (8) Morari, C.; Rungger, I.; Rocha, A. R.; Sanvito, S.; Melinte, S.; Rignanes, G.-M. Electronic Transport Properties of 1,1'-Ferrocene Dicarboxylic Acid Linked to Al(111) Electrodes. *ACS Nano* **2009**, *3*, 4137–4143.
- (9) Dinglasan, J. A. M.; Bailey, M.; Park, J. B.; Dhirani, A. A. Differential Conductance Switching of Planar Tunnel Junctions Mediated by Oxidation/Reduction of Functionally Protected Ferrocene. *J. Am. Chem. Soc.* **2004**, *126*, 6491–6497.
- (10) Ormaza, M.; Robles, R.; Bachellier, N.; Abufager, P.; Lorente, N.; Limot, L. On-Surface Engineering of a Magnetic Organometallic Nanowire. *Nano Lett.* **2016**, *16*, 588–593.
- (11) Bartels, L. Tailoring molecular layers at metal surfaces. *Nat. Chem.* **2010**, *2*, 87–95.
- (12) Gambardella, P.; Stepanow, S.; Dmitriev, A.; Honolka, J.; de Groot, F. M. F.; Lingenfelder, M.; Gupta, S. S.; Sarma, D. D.; Bencok, P.; Stanescu, S.; et al. Supramolecular control of the magnetic anisotropy in two-dimensional high-spin Fe arrays at a metal interface. *Nat. Mater.* **2009**, *8*, 189–193.
- (13) Barth, J. V.; Costantini, G.; Kern, K. Engineering atomic and molecular nanostructures at surfaces. *Nature* **2005**, *437*, 671–679.
- (14) Saha, P.; Yadav, K.; Chacko, S.; Philip, A. T.; Ramapanicker, R.; Gopakumar, T. G. Controlling Growth to One Dimension in Nanoislands of Ferrocene-Sugar Derivatives. *J. Phys. Chem. C* **2016**, *120*, 9223–9228.
- (15) Stepanow, S.; Lingenfelder, M.; Dmitriev, A.; Spillmann, H.; Delvigne, E.; Lin, N.; Deng, X.; Cai, C.; Barth, J. V.; Kern, K. Steering molecular organization and host-guest interactions using two-dimensional nanoporous coordination systems. *Nat. Mater.* **2004**, *3*, 229–233.
- (16) Chae, H. K.; Siberio-Perez, D. Y.; Kim, J.; Go, Y.; Eddaoudi, M.; Matzger, A. J.; O'Keeffe, M.; Yaghi, O. M. A route to high surface area, porosity and inclusion of large molecules in crystals. *Nature* **2004**, *427*, 523–527.
- (17) Jeffrey, G. A.; Jeffrey, G. A. *An introduction to hydrogen bonding*; Oxford University Press: New York, 1997; Vol. 12.
- (18) Wasio, N. A.; Quardokus, R. C.; Forrest, R. P.; Lent, C. S.; Corcelli, S. A.; Christie, J. A.; Henderson, K. W.; Kandel, S. A. Self-assembly of hydrogen-bonded two-dimensional quasicrystals. *Nature* **2014**, *507*, 86–89.
- (19) Cleaves, H. J. J. In *Encyclopedia of Astrobiology*; Gargaud, M., Amls, R., Quintanilla, J. C., Cleaves, H. J. J., Irvine, W. M., Pinti, D. L., Viso, M., Eds.; Springer: Berlin, 2011; Chapter Carboxylic Acid, pp 249–250.
- (20) Gross, L.; Mohn, F.; Moll, N.; Liljeroth, P.; Meyer, G. The Chemical Structure of a Molecule Resolved by Atomic Force Microscopy. *Science* **2009**, *325*, 1110–1114.
- (21) Hapala, P.; Temirov, R.; Tautz, F. S.; Jelinek, P. Origin of High-Resolution IETS-STM Images of Organic Molecules with Functionalized Tips. *Phys. Rev. Lett.* **2014**, *113*, 226101.
- (22) Hapala, P.; Kichin, G.; Wagner, C.; Tautz, F. S.; Temirov, R.; Jelinek, P. Mechanism of high-resolution STM/AFM imaging with functionalized tips. *Phys. Rev. B: Condens. Matter Mater. Phys.* **2014**, *90*, 085421.
- (23) Ma, X.-D.; Bazhanov, D. I.; Fruchart, O.; Yildiz, F.; Yokoyama, T.; Przybylski, M.; Stepanyuk, V. S.; Hergert, W.; Kirschner, J. Strain Relief Guided Growth of Atomic Nanowires in a Cu₃N–Cu(110) Molecular Network. *Phys. Rev. Lett.* **2009**, *102*, 205503.
- (24) Bhattacharjee, K.; Ma, X. D.; Zhang, Y. Q.; Przybylski, M.; Kirschner, J. Electronic structure of the corrugated Cu 3N network on Cu(110): Tunneling spectroscopy investigations. *Surf. Sci.* **2012**, *606*, 652–658.
- (25) Karis, O.; Hasselstrom, J.; Wassdahl, N.; Weinelt, M.; Nilsson, A.; Nyberg, M.; Pettersson, L. G. M.; Stohr, J.; Samant, M. G. The bonding of simple carboxylic acids on Cu(110). *J. Chem. Phys.* **2000**, *112*, 8146–8155.
- (26) González-Moreno, R.; Garcia-Lekue, A.; Arnau, A.; Trelka, M.; Gallego, J. M.; Otero, R.; Verdini, A.; Sánchez-Sánchez, C.; de Andrés, P. L.; Martín-Gago, J. Á.; et al. Role of the Anchored Groups in the Bonding and Self-Organization of Macrocycles: Carboxylic versus Pyrrole Groups. *J. Phys. Chem. C* **2013**, *117*, 7661–7668.
- (27) Herron, J. A.; Scaranto, J.; Ferrin, P.; Li, S.; Mavrikakis, M. Trends in Formic Acid Decomposition on Model Transition Metal Surfaces: A Density Functional Theory study. *ACS Catal.* **2014**, *4*, 4434–4445.
- (28) Blum, V.; Gehrke, R.; Hanke, F.; Havu, P.; Havu, V.; Ren, X.; Reuter, K.; Scheffler, M. Ab initio molecular simulations with numeric atom-centered orbitals. *Comput. Phys. Commun.* **2009**, *180*, 2175–2196.
- (29) Perdew, J. P.; Burke, K.; Ernzerhof, M. Generalized Gradient Approximation Made Simple. *Phys. Rev. Lett.* **1996**, *77*, 3865–3868.
- (30) Tkatchenko, A.; Scheffler, M. Accurate Molecular Van Der Waals Interactions from Ground-State Electron Density and Free-Atom Reference Data. *Phys. Rev. Lett.* **2009**, *102*, 073005.

Characteristic Contrast in Δf_{\min} Maps of Organic Molecules Using Atomic Force Microscopy

Nadine J. van der Heijden,[†] Prokop Hapala,[‡] Jeroen A. Rombouts,[§] Joost van der Lit,[†] Daniël Smith,[†] Pingo Mutombo,[‡] Martin Švec,[‡] Pavel Jelinek,[‡] and Ingmar Swart^{*,†}

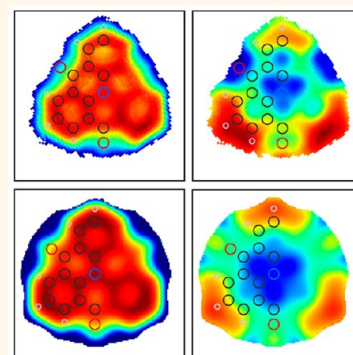
[†]Condensed Matter and Interfaces, Debye Institute for Nanomaterials Science, Utrecht University, P.O. Box 80000, 3508 TA Utrecht, The Netherlands

[‡]Institute of Physics, Czech Academy of Sciences, Cukrovarnická 10, 1862 53 Prague, Czech Republic

[§]Department of Chemistry and Pharmaceutical Sciences, VU University Amsterdam, De Boelelaan 1083, 1081 HV Amsterdam, The Netherlands

S Supporting Information

ABSTRACT: Scanning tunneling microscopy and atomic force microscopy can provide detailed information about the geometric and electronic structure of molecules with submolecular spatial resolution. However, an essential capability to realize the full potential of these techniques for chemical applications is missing from the scanning probe toolbox: chemical recognition of organic molecules. Here, we show that maps of the minima of frequency shift–distance curves extracted from 3D data cubes contain characteristic contrast. A detailed theoretical analysis based on density functional theory and molecular mechanics shows that these features are characteristic for the investigated species. Structurally similar but chemically distinct molecules yield significantly different features. We find that the van der Waals and Pauli interaction, together with the specific adsorption geometry of a given molecule on the surface, accounts for the observed contrast.



KEYWORDS: AFM, DFT, molecular mechanics, single molecule, CO tip, Xe tip

Scanning tunneling microscopy (STM) and atomic force microscopy (AFM) are both capable of imaging molecules with submolecular resolution.^{1–5} In addition, both techniques can provide quantitative information: STM on the electronic structure and AFM on the charge distribution and the bond orders.^{5–8} Hence, both techniques find increasing use in the field of chemistry. To realize the full potential of STM and AFM in studies involving molecules, the ability to identify or recognize molecules is of great value. STM provides chemical recognition capabilities *via* inelastic electron tunneling spectroscopy *via* differences in the local density of states and vibration frequencies of bonds.^{9–12} Force–distance spectroscopy, combined with density functional theory (DFT) calculations, has been used to chemically identify atoms in surfaces of insulators, alloys, and semiconductors.^{13–19} In most cases, the origin of the chemical contrast is due to formation of atom-specific covalent bonds with the tip. However, submolecular resolution imaging of molecules requires the use of chemically passivated tips to avoid an accidental pickup of the molecule of interest. Hence, chemical recognition of atoms within an organic molecule has to rely on a different contrast mechanism. Contrast differences in AFM images over various chemical elements in organic molecules have been observed, indicating that elemental identification may be possible.^{20–22} Thus far, chemical recognition with AFM has mostly relied on structural arguments.^{20–22}

The chemical identification procedure for atoms in an alloy surface¹⁴ cannot be transferred to recognize organic molecules adsorbed on a surface. First, the chemical contrast observed on surfaces is due to the formation of a (partial) covalent bond between the reactive metal tip and the atoms under investigation. This is in direct conflict with the requirement to use chemically passivated tips. Another complication that hampers direct chemical identification of atoms in molecules by comparing frequency shift–distance ($\Delta f(z)$) spectra is the fact that the van der Waals (vdW) force varies strongly over a single molecule on a surface.²³ Hence, $\Delta f(z)$ spectra acquired over identical elements in a molecule, one at the center and the other at the periphery, will be significantly different. This is especially important because for most organic molecules the majority of the atoms reside at the periphery. However, it is important to realize that chemical recognition of molecules does *not* require each atom in a molecule to be identified separately. Instead, it is sufficient if the molecule as a whole exhibits some characteristic contrast. Since the overall magnitude and shape of the potential energy landscape experienced by the tip should reflect both the geometry

Received: June 2, 2016

Accepted: August 10, 2016

Published: August 10, 2016

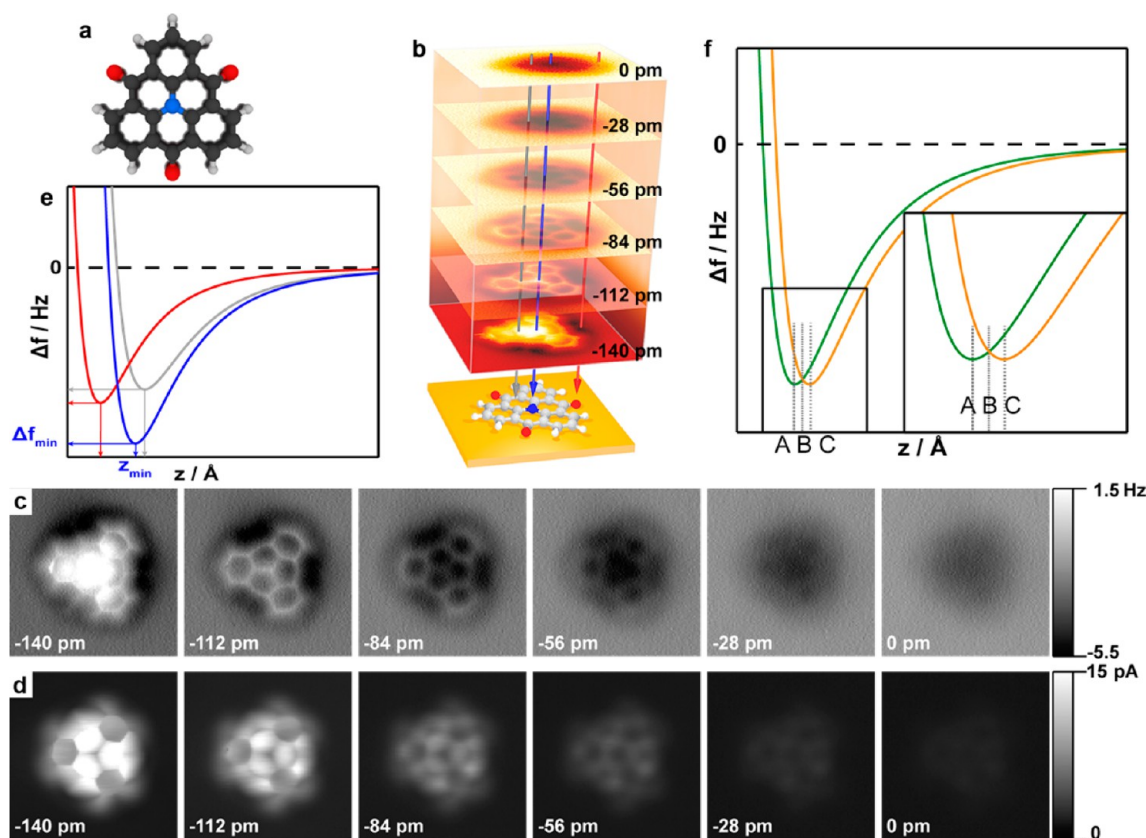


Figure 1. Acquisition and analysis of a 3D Δf data cube over a model molecule. (a) Model of 1,5,9-trioxo-13-azatriangulene, which consists of carbon (black), nitrogen (blue), oxygen (red), and hydrogen (white) atoms. (b,c) Selection of constant height AFM images acquired with a CO-terminated tip. Indicated heights are with regard to an STM set point of 10 pA at 100 mV. (d) Simultaneously recorded current images. (e) $\Delta f(z)$ spectra can be extracted from the stack of constant height images shown in (b,c), indicated here by model curves (*i.e.*, the curves shown here do not represent experimental data). (f) Schematic curves with an offset in the vertical position of the minimum frequency shift, z_{\min} , which may correspond to spectra acquired over different sites in a molecule.

and the chemical composition of the molecule, it may be possible to chemically recognize molecules on surfaces with AFM.

Here, we present a proof-of-concept study that demonstrates that maps of the minima of $\Delta f(z)$ curves, that is, maps of $z_{\min}(x,y)$ and of $\Delta f_{\min}(x,y)$, acquired over a molecule exhibit characteristic contrast. This contrast is reproduced in simulations based on molecular mechanics (MM) and DFT. We show that the vdW and Pauli interaction, together with the specific adsorption geometry of a given molecule on the surface, accounts for the observed contrast.

RESULTS AND DISCUSSION

We synthesized a planar three-fold rotationally symmetric model molecule, 1,5,9-trioxo-13-azatriangulene (TOAT) (Figure 1a), that contains H, C, N, and O atoms. The planarity eliminates effects due to vertical corrugation.²⁴ This model molecule was prepared using an established synthesis scheme.^{25,26}

The 3D Δf maps were acquired with CO-terminated tips by measuring stacks of 100 constant height AFM images with an interval of 7 pm over TOAT adsorbed on Cu(111). The image at the smallest tip-sample distance was taken at $\Delta z = -140$ pm with respect to an STM set point of $I = 10$ pA at $V = 0.1$ V. A selection from the experimental AFM images is shown in Figure 1b,c. In addition, Figure 1d shows the corresponding simultaneously recorded current images. The geometric structure of the molecule is clearly resolved. We extracted experimental $\Delta f(z)$ spectra over the molecule from the 3D data cube,

as schematically illustrated in Figure 1b,e, from which we determined the $z_{\min}(x,y)$ and $\Delta f_{\min}(x,y)$ maps.

Before discussing these maps, we briefly discuss the advantage of acquiring and analyzing a 3D data grid over regular constant height images. The contrast in constant height AFM images sensitively depends on the height. However, also the *difference* in the contrast between sites can change as a function of tip-sample distance. For example, consider the two schematic $\Delta f(z)$ curves shown in Figure 1f. These could correspond to curves acquired over different sites in the molecule. Constant height images taken at tip-sample distances A and C will show an inverted contrast. Furthermore, if an image is taken at tip-sample distance B, the contrast at the two positions where the curves were acquired is identical. Since $\Delta f(z)$ curves—and their spatial variation—are not *a priori* known, it is impossible to know at which tip-sample distance to take an image. In contrast, $z_{\min}(x,y)$ and $\Delta f_{\min}(x,y)$ maps provide robust information.

The experimental work is complemented by a theoretical analysis. First, the adsorption geometry and charge distribution of TOAT on Cu(111) were calculated using total energy DFT simulations including vdW interactions. The relaxed geometry of the molecule on the surface is shown in Figure 2. Details can be found in the Supporting Information. The DFT results (charge distribution, adsorption geometry) were used as input for the MM-based simulation of the full 3D AFM data. The methods used in this second step have been described in detail elsewhere.^{8,27–29} The mechanistic model includes the vdW and

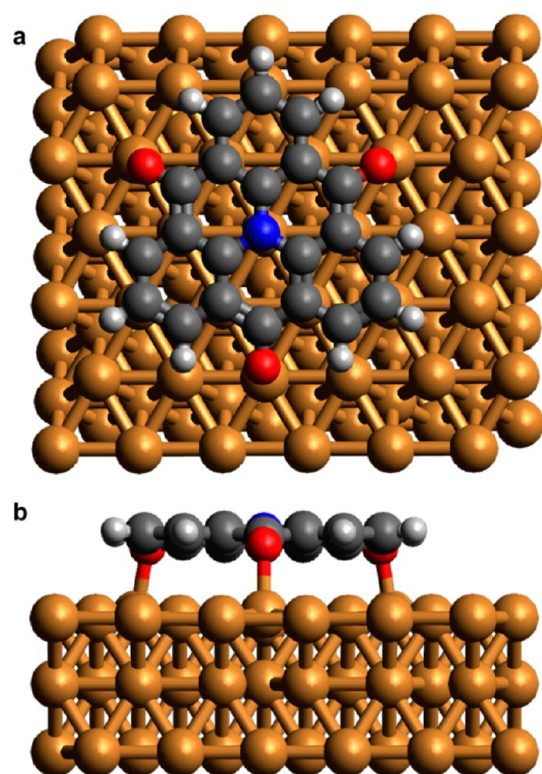


Figure 2. Fully relaxed atomic structure of TOAT on Cu(111) obtained from periodic DFT calculations including van der Waals interactions. (a) Top view. (b) Side view.

Pauli forces, as well as the electrostatic interactions between the tip and sample. The two main parameters in the mechanistic model are the lateral stiffness (k) of the probe particle–bulk tip

junction and the effective charge (Q) of the probe particle. The parameters that provide the best agreement with experimental data were determined by comparing a stack of images simulated with different values of k and Q with experimental AFM images acquired at different heights above the molecule as described previously.⁸ The as-determined values are $k = 0.24$ N/m and $Q = 0.0e^-$. These values are in fair agreement with previously reported values.^{7,30,31} We note here that the effective charge of the CO will depend on how the molecule is adsorbed on the tip as well as on the chemical composition of the metallic tip apex to which it is bound. In addition, we added a long-range $\Delta f(z)$ component, estimated from experimental $\Delta f(z)$ spectra taken on the bare Cu(111) surface, to enable a direct comparison between the experimental and theoretical data.

The minima of the experimental and simulated $\Delta f(z)$ curves were found by fitting a parabola to points up to 1 Hz above the most negative Δf value. Over the lower lying Cu(111) substrate, the $\Delta f(z)$ spectra did not reach the minimum, which could therefore not be assigned. Contour plots of the as-determined values of experimental and simulated $z_{\min}(x,y)$ and $\Delta f_{\min}(x,y)$ maps are plotted in Figure 3a–d. Using the coordinates of the minimum of the curve to compare experimental data to simulated images enables us to review detailed information and small deviations visually. Extracting the location of the minimum from a $\Delta f(z)$ curve yields information about the effect and interplay of both repulsive and attractive forces. Alternatively, one can extract Lennard-Jones fit parameters from $\Delta f(z)$ spectra, but these are more prone to errors due to tip flexibility, especially at close distance. At distances where $z_{\min}(x,y)$ and $\Delta f_{\min}(x,y)$ are located, the lateral relaxation of the probe is still negligible.

The experimental and simulated $z_{\min}(x,y)$ and $\Delta f_{\min}(x,y)$ maps, shown in Figure 3, are overall in good agreement. Another set of maps, acquired with a different CO-terminated tip on a different molecule, is shown in the Supporting Information.

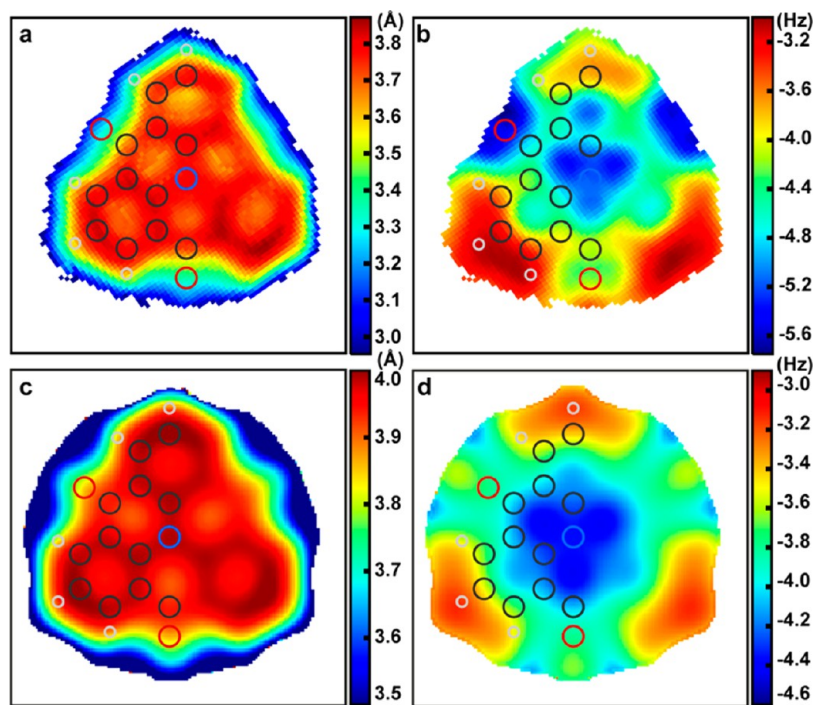


Figure 3. (a) Experimental $z_{\min}(x,y)$ and (b) $\Delta f_{\min}(x,y)$ maps, obtained with a CO-terminated tip. (c) Calculated $z_{\min}(x,y)$ and (d) $\Delta f_{\min}(x,y)$ maps. Theoretical $\Delta f_{\min}(x,y)$ and $z_{\min}(x,y)$ maps are calculated using a lateral stiffness $k = 0.24$ N/m and an effective charge on the CO tip of $Q = 0.0e^-$.

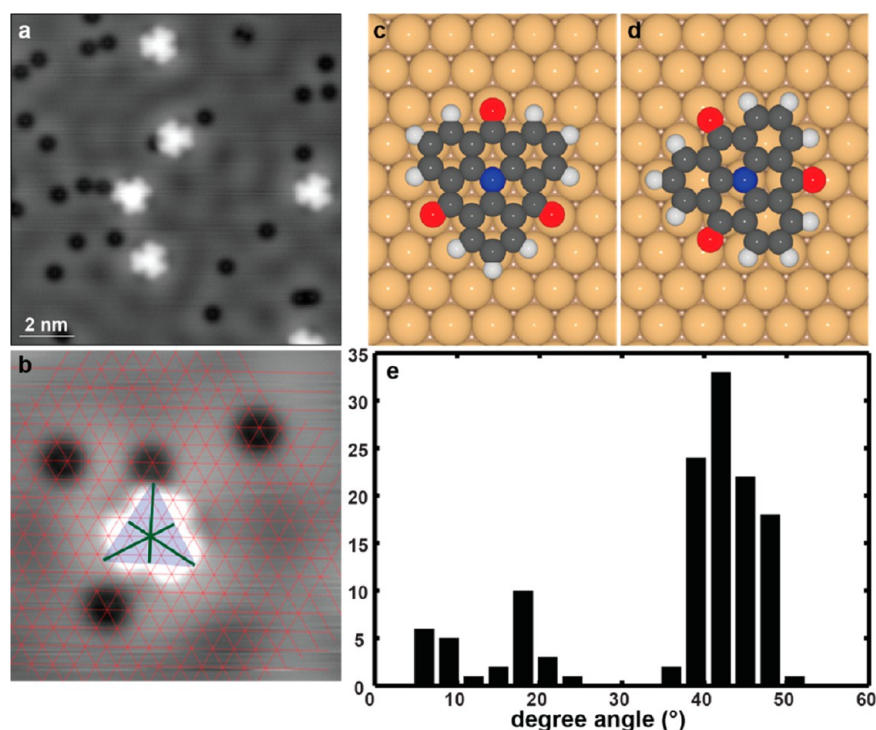


Figure 4. Study of adsorption orientation of TOAT on Cu(111). (a) STM image of six TOAT molecules and several CO molecules on Cu(111), acquired with a CO-terminated tip. (b) STM image of an adsorbed TOAT molecule and surrounding CO molecules, acquired with a CO-terminated tip. The dimensions of the overlaid grid correspond to the atomic configuration of the Cu(111) surface. (c,d) Schematic representation of a TOAT molecule adsorbed on Cu(111) between rows and along row orientations, respectively. (e) Histogram of relative angles of adsorbed TOAT molecules.

Above bonds/atoms, $z_{\min}(x,y)$ is located at larger values of z compared to other positions (values of z refer to the height above the molecular plane). This is expected because, at these positions, repulsive interactions become more important at smaller tip-sample distances. Hence, the $z_{\min}(x,y)$ maps resemble the structure of the molecule, including vertical corrugation within the molecule. The $\Delta f_{\min}(x,y)$ maps feature more contrast. Above the benzene rings at the periphery, the minimum of the frequency shift is less negative (red) compared to the center of the molecule (blue). This is ascribed to the smaller vdW attraction at the edges. Note that the experimental maps do not extend as far outward from the center of the molecule as the simulated maps. Using an alternative approach, it should be possible to create $z_{\min}(x,y)$ and $\Delta f_{\min}(x,y)$ maps of the entire imaging area.³² Our total energy calculations indicate a very shallow potential energy with respect to the vertical distortion of the oxygen atoms. The resulting uncertainty in the vertical position of the oxygen atoms will affect the contrast at these positions (see [Supporting Information](#)).

The contrast in the experimental $\Delta f_{\min}(x,y)$ map has an imperfect three-fold symmetry. There can be multiple reasons for this. To investigate if this imperfect symmetry in the maps is due to a reduction of the symmetry induced by adsorption on the surface, we determined the adsorption configurations. We find that TOAT adsorbs on Cu(111) with two different orientations, rotated by 30°; see [Figure 4](#). The adsorption configurations of both species was determined by using coevaporated CO molecules as markers (CO molecules are known to be adsorbed on top of Cu atoms³³). An example is shown in [Figure 4b](#). An analysis of multiple molecules consistently shows that in both configurations the N atom is adsorbed on top of a Cu atom. The two configurations correspond to molecules with their O atoms pointing between and along rows of Cu atoms ([Figure 4c,d](#),

respectively). Both of these adsorption geometries are three-fold symmetric. The imperfect symmetry in the experimental $\Delta f_{\min}(x,y)$ map is therefore attributed to tip flexibility in conjunction with an asymmetric tip (on the mesoscopic scale).^{19,29,34} This is further supported by the fact that maps acquired with a different CO-terminated tip on a different molecule exhibit a different symmetry (see [Supporting Information](#)).

To further investigate if the observed contrast in the $\Delta f_{\min}(x,y)$ and $z_{\min}(x,y)$ maps are molecule-specific, we take advantage of the good agreement of the simulated and experimental data. We calculated $\Delta f_{\min}(x,y)$ and $z_{\min}(x,y)$ maps with a CO tip for molecules with a different chemical composition but a similar structure. Specifically, we replaced the ketone groups by an ether (TOAT-ether) or a secondary amine (TOAT-amine), or we replaced the central N with a C (TOAT-C); see [Figure 5a–c](#). In the latter case, one of the O atoms is changed into a hydroxyl group (OH) to maintain charge neutrality. Note that these molecules all have the same skeleton of conjugated carbon rings. However, each molecule has a distinct contrast in the $\Delta f_{\min}(x,y)$ and $z_{\min}(x,y)$ maps, and they are different from the maps of TOAT shown in [Figure 3](#). Our DFT calculations revealed that these differences originate from different vdW interactions, as well as from changes in the atomic relaxation of the molecules on the surface.²⁶ This is in agreement with the observation of Schuler *et al.* that polycyclic aromatic hydrocarbons that have a different functional group have a different adsorption height.³⁵

The $\Delta f_{\min}(x,y)$ maps also exhibit clear differences, especially at the periphery, where the different functional groups are located. In particular, there is a shift in location and depth of the well, indicated by green arrows in [Figure 5g–i](#). The calculated $\Delta f_{\min}(x,y)$ of TOAT-C ([Figure 4f](#)) contains an asymmetry caused by the OH group on the periphery. From this

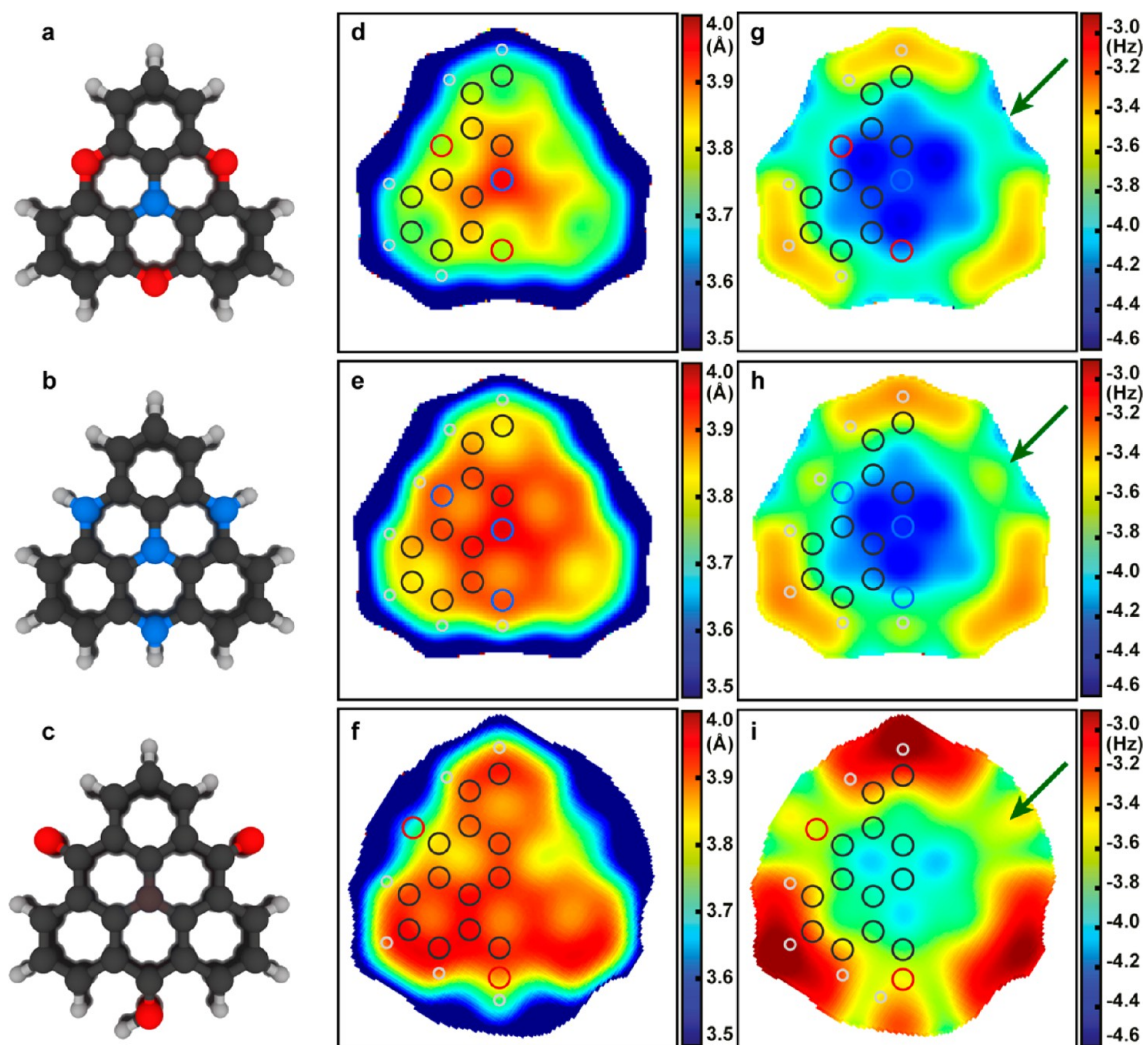


Figure 5. Schematic representations of theoretically investigated molecules, where ketone groups in TOAT are replaced by (a) an ether (TOAT-ether), (b) a secondary amine (TOAT-amine), (c) the central N with a C (TOAT-C). Calculated $z_{\min}(x,y)$ maps for (d) TOAT-ether, (e) TOAT-amine, (f) TOAT-C. Calculated $\Delta f_{\min}(x,y)$ maps for (g) TOAT-ether, (h) TOAT-amine, (i) TOAT-C. Theoretical $\Delta f_{\min}(x,y)$ and $z_{\min}(x,y)$ are calculated with a lateral stiffness of $k = 0.24$ N/m and an effective charge on the CO tip of $Q = 0.0e^-$.

comparison, it is evident that $\Delta f_{\min}(x,y)$ and $z_{\min}(x,y)$ maps can be used to discriminate between molecules.

We now turn our attention to the origin of the characteristic contrast. Since the simulations without including electrostatic forces (the effective charge Q on the tip is zero) can reproduce the experimental observations very well, electrostatic forces cannot be responsible for the characteristic contrast. Hence, the vdW and Pauli interaction, together with the specific adsorption geometry of a given molecule on the surface, must therefore account for the contrast. At the distance of most negative frequency shift, that is, at the z corresponding to Δf_{\min} , the vdW component is dominant.

Considering that discussed above, the contrast in the $z_{\min}(x,y)$ and $\Delta f_{\min}(x,y)$ maps may be blurred for probes with a large atomic radius (e.g., Xe) and/or a significant charge. A larger probe radius leads to increased interactions with neighboring atoms, resulting in an averaging effect. Charged tips may not be suitable since the charge distribution in molecules typically varies rather slowly, and regions of increased charge density are not necessarily localized on atoms. We note here that the large majority of the molecules have a nonhomogeneous charge distribution.

To support this interpretation of the contrast mechanism, we repeated the experiment and simulations with a positively charged Xe-terminated tip (parameters: $Q = +0.3e^-$ and $k = 0.24$ N/m).⁸ A selection from the constant height AFM images and the corresponding I images is shown in Figure 6.

Figure 7 shows the experimental and theoretical $z_{\min}(x,y)$ and $\Delta f_{\min}(x,y)$ maps extracted from the 3D data. The simulated and experimental maps show, just like for the CO tip, very good agreement. However, in contrast to the maps acquired with CO tips, both $\Delta f_{\min}(x,y)$ and $z_{\min}(x,y)$ maps acquired with Xe-terminated tips show very little features. Our theoretical analysis shows that the loss of resolution is driven by both (i) the large atomic radius of Xe and (ii) the pronounced electrostatic interaction between the charged probe and the molecule. Because of these two reasons, Xe-terminated tips are less suitable for chemical recognition of molecules.

The C and N atoms in the center of the molecule have a similar chemical and geometric environment. In addition, the gradient of the underlying vdW background is small in the interior of the molecule. Furthermore, their central location is important to minimize the influence of tip relaxations (i.e., bending of the CO).²⁴ Hence, for this molecule, $\Delta f(z)$ spectra acquired above C

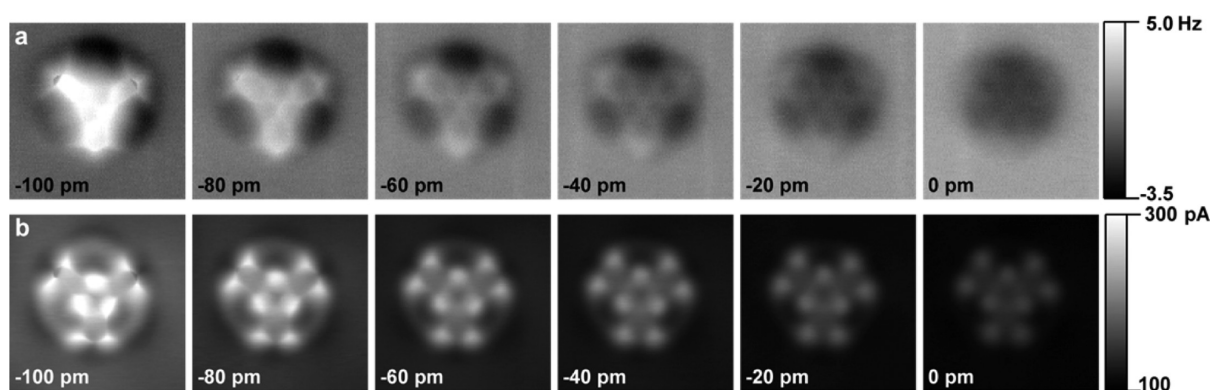


Figure 6. Selection of images from 3D mapping, recorded with a Xe-terminated tip. (a) Selection of constant height AFM images. (b) Simultaneously recorded I images. Indicated heights are with regard to STM set point of 500 pA at 200 mV.

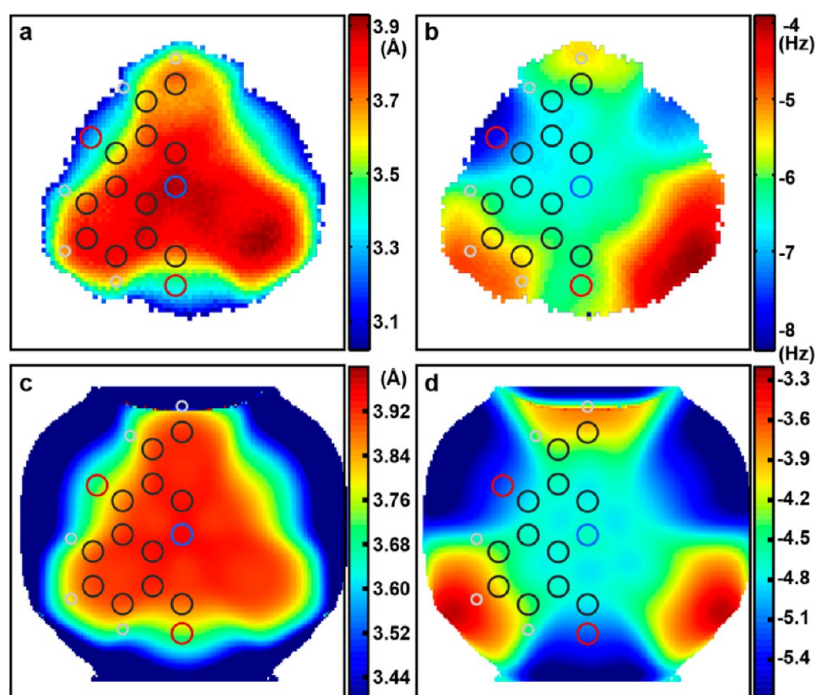


Figure 7. (a) Experimental $z_{\min}(x,y)$ and (b) $\Delta f_{\min}(x,y)$ maps, obtained with a Xe-terminated tip. (c) Calculated $z_{\min}(x,y)$ and (d) $\Delta f_{\min}(x,y)$ maps. Theoretical $\Delta f_{\min}(x,y)$ and $z_{\min}(x,y)$ are calculated with a lateral stiffness of $k = 0.24$ N/m and an effective charge on the Xe tip of $Q = +0.3e^-$.

and N in the center can be compared on (almost) equal footing. Figure 8a shows $\Delta f(z)$ spectra extracted from the same 3D data set as was used to compile the $\Delta f_{\min}(x,y)$ and $z_{\min}(x,y)$ maps in Figure 3. The (x,y) positions approximately correspond to the location of a N (blue) and three equivalent C (black) atoms, respectively (see inset). The coordinates of the minimum are distinctly different for the different atoms: the well above the central N atom (blue curve) is deeper than that above a C atom (black curve). The value of z_{\min} for both atoms is the same within experimental error, indicating that they have the same adsorption height to within a few picometers. This is in good agreement with the DFT calculations. The differences between the chemically and geometrically equivalent C atoms are much smaller than the difference between C and N. The calculated $\Delta f(z)$ spectra over these atoms are shown in Figure 8b and reproduce the experimentally observed trend.

To examine the influence of the adsorption site on the $\Delta f(z)$ curves, spectra were simultaneously acquired above molecules in both configurations. Figure 8c shows a constant height AFM

image of two molecules with different adsorption configuration. As shown in Figure 8d, spectra acquired over equivalent positions over the two molecules overlap within experimental error. Note that the trend is the same as observed in the spectra extracted from the 3D data cube: Δf_{\min} is significantly more negative for N than for the neighboring C atoms. This trend should hold for all tertiary amines (N atom coordinated to three C atoms) and C atoms that have a similar geometric and chemical environment (including adsorption height and interaction with the surface). The absolute values differ between experiments due to different macroscopic atomic tip clusters, resulting in different vdW contributions.

CONCLUSION

In summary, we showed that maps of $z_{\min}(x,y)$ and $\Delta f_{\min}(x,y)$ acquired with CO-terminated tips have distinct characteristics that can differentiate between structurally similar molecules on surfaces. The characteristic contrast in these maps originates from the vdW interactions between tip and molecule, as well as

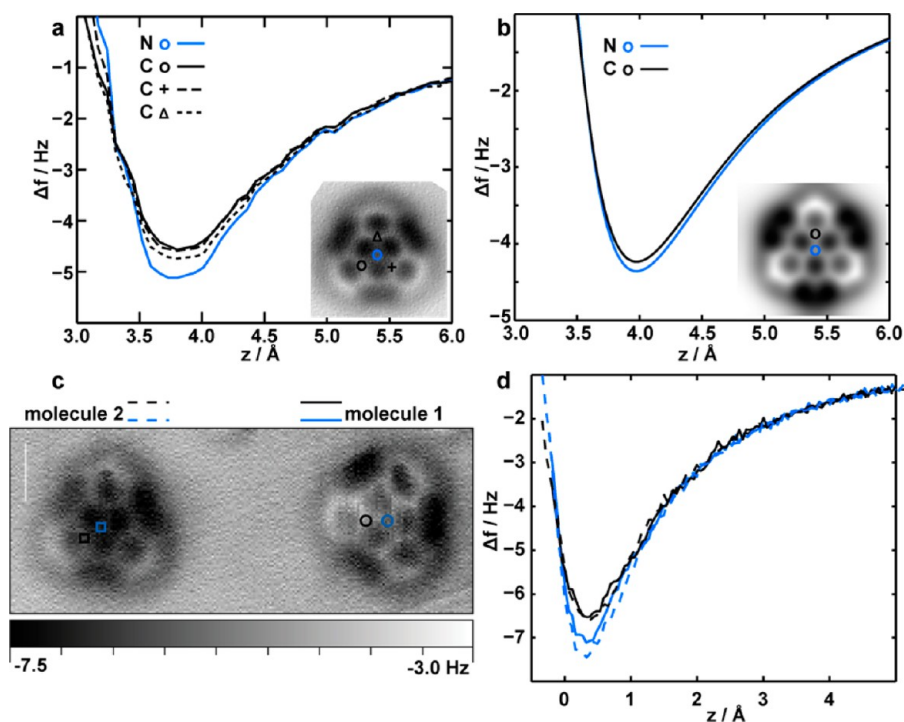


Figure 8. Additional $\Delta f(z)$ spectra over TOAT molecules with CO-terminated tips. (a) $\Delta f(z)$ spectra extracted from the 3D data grid over selected positions on TOAT, as indicated in the inset. The $\Delta f(z)$ spectra are the average of nine curves of a 3×3 pixel area; *i.e.*, each spectrum is the average of the spectra of the selected pixel and the pixels touching the selected one. (b) Calculated $\Delta f(z)$ spectra extracted over selected positions on TOAT, as indicated in the inset. (c) Constant height AFM image of two molecules in different orientation, at -130 pm with regard to the STM set point of 10 pA at 100 mV. Molecule 1 and molecule 2 lie with their peripheral O atoms between and along atomic rows, respectively. (d) Individual $\Delta f(z)$ spectra acquired above the same atoms as in (a) and (b) over the two molecules in (c), where $z = 0$ Å corresponds to the imaging height of (c). The z values of molecule 1 are corrected for z -drift using the following procedure. Immediately prior to the AFM experiment, an $I(z)$ curve was acquired (with the same oscillation amplitude and bias). These data were used to convert the observed changes in the tunnel current during the constant height experiment to a change in tip–sample distance. The z -drift between acquisition of the two $\Delta f(z)$ spectra was 0.35 Å.

from the adsorption geometry of the molecule on the surface. Since the adsorption height (and its variations within a molecule) strongly depend on the interaction between the molecule and the substrate, the $z_{\min}(x,y)$ and $\Delta f_{\min}(x,y)$ maps of a particular molecule should be substrate-dependent. The trends in z position and the depth of the minimum are the same for all CO-terminated tips, while the absolute values differ from tip to tip. Tips employing larger atoms and/or tips with a significant charge (like Xe) are less suitable for chemical recognition of molecules.

The force resolution required to apply the procedure outlined here is on the order of 1 pN/100 mHz (for a typical qPlus sensor). This criterion is typically fulfilled in cases where submolecular resolution imaging of molecules has been reported.

METHODS

Synthesis of 1,5,9-Trioxo-13-azatriangulene. The synthesis reported herein is based on literature procedures.²⁵ For the sake of completeness and reproducibility, we describe the procedure and our observations. The first step is the synthesis of tris(*ortho*-methylbenzoate)-amine (TOMBA). TOMBA was synthesized by refluxing a solution in diphenyl ether of 1:3:2 parts of 2-aminobenzoic acid methyl ester, 2-iodobenzoic acid methyl ester, and potassium carbonate, respectively, in the presence of copper and copper(I) iodide, for 16 h at 210 °C under nitrogen atmosphere. After purification, the yield was 76%. The purified TOMBA was subsequently used to synthesize TOAT. A solution of TOMBA in 98% H_2SO_4 was heated to 105 °C and kept at that temperature for 24 h. After purification, the yield was 7.2% (46.9 mg). Further details of the synthesis, purification, and spectra can be found in the Supporting Information.²⁶

STM and AFM Measurements. We used an Omicron Nanotechnology LT STM/AFM with a commercially available qPlus sensor, operating at approximately 4.6 K in ultrahigh vacuum with an average pressure of 5×10^{-10} mbar. A Cu(111) crystal surface was cleaned with several sputter and anneal cycles before being inserted into the microscope head. The TOAT molecules were thermally evaporated onto the cold surface using a Knudsen cell-type evaporator. For STM imaging, the bias voltage was applied to the sample. The baked qPlus sensor (3 h at 120 °C) had a quality factor of $Q \approx 30\,000$, a resonance frequency of $f_0 = 25\,634$ Hz, and a peak-to-peak oscillation amplitude of <2 Å. After the tip approached the surface, it often needed some preparation to sharpen the apex and ensure stability. This was accomplished with controlled crashes into the copper surface and bias pulses until the STM resolution was satisfactory. The tip apex was functionalized with a single CO molecule following the standard method.³⁶ After an appropriate TOAT molecule was located on the surface, the tip was left in tunneling contact ($I = 10$ pA at $V = 0.1$ V) and allowed to relax for 12 h to prevent drift and creep. After this time, there was no detectable x - or y -drift. To compensate for z -drift, the STM feedback was turned on for 2 s after each constant height AFM image and then turned off again before adjusting the height for the next image. No data analysis procedures such as those described in ref 37 were therefore necessary. The AFM was operated in constant height mode, and AFM images show the frequency shift (Δf) with respect to the resonance frequency.

Specific acquisition parameters for the maps presented in this article are as follows. The stack resulting in the maps of Figure 4 consisted of 100 images, from -140 pm to $+553$ pm with regard to an STM set point of 10 pA at 100 mV, in steps of 7 pm. The spectra in Figure 8a were extracted from this stack. The stack resulting in the maps of Figure 7 had 35 images, from -100 pm to $+75$ pm with regard to an STM set point of 500 pA at 200 mV.

Theoretical Modeling. Simulations were performed using MM calculations using geometries and charge distributions as determined from DFT calculations.²⁶

ASSOCIATED CONTENT

Supporting Information

The Supporting Information is available free of charge on the ACS Publications website at DOI: 10.1021/acsnano.6b03644.

Synthesis of 1,5,9-trioxo-13-azatriangulene, brief description of DFT modeling, brief description of the mechanical probe particle AFM model (PDF)

AUTHOR INFORMATION

Corresponding Author

*E-mail: i.swart@uu.nl.

Notes

The authors declare no competing financial interest.

ACKNOWLEDGMENTS

We thank Daniël Vanmaekelbergh for valuable discussions. Financial support from the Nederlandse Organisatie voor Wetenschappelijk Onderzoek (ECHO-Stip Grant No. 717.013.003), the GACR (Project No. 14-16963J), and the BioSolar Cells Program of the Dutch Ministry of Economic Affairs is gratefully acknowledged.

REFERENCES

- (1) Repp, J.; Meyer, G.; Stojković, S. M.; Gourdon, A.; Joachim, C. Molecules on Insulating Films: Scanning-Tunneling Microscopy Imaging of Individual Molecular Orbitals. *Phys. Rev. Lett.* **2005**, *94*, 26803.
- (2) Gross, L.; Mohn, F.; Moll, N.; Liljeroth, P.; Meyer, G. The Chemical Structure of a Molecule Resolved by Atomic Force Microscopy. *Science* **2009**, *325*, 1110–1114.
- (3) Weiss, C.; Wagner, C.; Tautz, F. S.; Temirov, R. Direct Imaging of Intermolecular Bonds in Scanning Tunneling Microscopy. *J. Am. Chem. Soc.* **2010**, *132*, 11864.
- (4) Chiang, C.-I.; Xu, C.; Han, Z.; Ho, W. Real-Space Imaging of Molecular Structure and Chemical Bonding by Single-Molecule Inelastic Tunneling Probe. *Science* **2014**, *344*, 885–888.
- (5) Mohn, F.; Gross, L.; Moll, N.; Meyer, G. Imaging the Charge Distribution within a Single Molecule. *Nat. Nanotechnol.* **2012**, *7*, 227–231.
- (6) Gross, L.; Moll, N.; Mohn, F.; Curioni, A.; Meyer, G.; Hanke, F.; Persson, M. High-Resolution Molecular Orbital Imaging Using a P-Wave STM Tip. *Phys. Rev. Lett.* **2011**, *107*, 86101.
- (7) Gross, L.; Mohn, F.; Moll, N.; Schuler, B.; Criado, A.; Guitian, E.; Pena, D.; Gourdon, A.; Meyer, G.; Guitián, E.; et al. Bond-Order Discrimination by Atomic Force Microscopy. *Science* **2012**, *337*, 1326–1329.
- (8) Hapala, P.; Svec, M.; van der Heijden, N. J.; van der Lit, J.; Stetsovych, O.; Ondráček, M.; Mutombo, P.; Swart, I.; Jelinek, P. Mapping the Electrostatic Force Field of Single Molecules from High-Resolution Scanning Probe Images. *Nat. Commun.* **2016**, *7*, 11560.
- (9) Stipe, B. C. Single-Molecule Vibrational Spectroscopy and Microscopy. *Science* **1998**, *280*, 1732–1735.
- (10) Schmid, M.; Stadler, H.; Varga, P. Direct Observation of Surface Chemical Order by Scanning Tunneling Microscopy. *Phys. Rev. Lett.* **1993**, *70*, 1441–1444.
- (11) Varga, P.; Schmid, M. Chemical Discrimination on Atomic Level by STM. *Appl. Surf. Sci.* **1999**, *141*, 287–293.
- (12) Jiang, J.; Kula, M.; Luo, Y. Molecular Modeling of Inelastic Electron Transport in Molecular Junctions. *J. Phys.: Condens. Matter* **2008**, *20*, 374110.
- (13) Lantz, M. A.; Hug, H. J.; Hoffmann, R.; van Schendel, P. J. A.; Kappenberger, P.; Martin, S.; Baratoff, A.; Güntherodt, H. J. Quantitative Measurement of Short-Range Chemical Bonding Forces. *Science* **2001**, *291*, 2580–2583.
- (14) Sugimoto, Y.; Pou, P.; Abe, M.; Jelinek, P.; Perez, R.; Morita, S.; Custance, O. Chemical Identification of Individual Surface Atoms by Atomic Force Microscopy. *Nature* **2007**, *446*, 64–67.
- (15) Setvín, M.; Mutombo, P.; Ondráček, M.; Majzik, Z.; Švec, M.; Cháb, V.; Ošťádal, I.; Sobotík, P.; Jelinek, P. Chemical Identification of Single Atoms in Heterogeneous III–IV Chains on Si(100) Surface by Means of Nc-AFM and DFT Calculations. *ACS Nano* **2012**, *6*, 6969–6976.
- (16) Teobaldi, G.; Lammle, K.; Trevelyan, T.; Watkins, M.; Schwarz, A.; Wiesendanger, R.; Shluger, A. L. Chemical Resolution at Ionic Crystal Surfaces Using Dynamic Atomic Force Microscopy with Metallic Tips. *Phys. Rev. Lett.* **2011**, *106*, 216102.
- (17) Welker, J.; Weymouth, A. J.; Giessibl, F. J. The Influence of Chemical Bonding Configuration on Atomic Identification by Force Spectroscopy. *ACS Nano* **2013**, *7*, 7377–7382.
- (18) Baykara, M. Z.; Todorović, M.; Mönig, H.; Schwendemann, T. C.; Ünverdi, Ö.; Rodrigo, L.; Altman, E. I.; Pérez, R.; Schwarz, U. D. Atom-Specific Forces and Defect Identification on Surface-Oxidized Cu(100) with Combined 3D-AFM and STM Measurements. *Phys. Rev. B: Condens. Matter Mater. Phys.* **2013**, *87*, 155414.
- (19) Hölscher, H.; Langkat, S. M.; Schwarz, a.; Wiesendanger, R. Measurement of Three-Dimensional Force Fields with Atomic Resolution Using Dynamic Force Spectroscopy. *Appl. Phys. Lett.* **2002**, *81*, 4428–4430.
- (20) Gross, L.; Mohn, F.; Moll, N.; Meyer, G.; Ebel, R.; Abdel-Mageed, W. M.; Jaspars, M. Organic Structure Determination Using Atomic-Resolution Scanning Probe Microscopy. *Nat. Chem.* **2010**, *2*, 821–825.
- (21) Schuler, B.; Meyer, G.; Peña, D.; Mullins, O. C.; Gross, L. Unraveling the Molecular Structures of Asphaltenes by Atomic Force Microscopy. *J. Am. Chem. Soc.* **2015**, *137*, 9870–9876.
- (22) Kawai, S.; Saito, S.; Osumi, S.; Yamaguchi, S.; Foster, A. S.; Spijker, P.; Meyer, E. Atomically Controlled Substitutional Boron-Doping of Graphene Nanoribbons. *Nat. Commun.* **2015**, *6*, 8098.
- (23) Moll, N.; Gross, L.; Mohn, F.; Curioni, A.; Meyer, G. The Mechanisms Underlying the Enhanced Resolution of Atomic Force Microscopy with Functionalized Tips. *New J. Phys.* **2010**, *12*, 125020.
- (24) Boneschanscher, M. P.; Hämäläinen, S. K.; Liljeroth, P.; Swart, I. Sample Corrugation Affects the Apparent Bond Lengths in Atomic Force Microscopy. *ACS Nano* **2014**, *8*, 3006–3014.
- (25) Hellwinkel, D.; Melan, M. Heteropolycyclen Vom Triangulentypp, I. 8.12-Dihydro-4H-benzo[1.9]chinolizino[3.4.5.6.7-Defg]acridin-Trion-(4.8.12) Und 5.9-Dihydro-chino[3.2.1-De]acridin-Dion-(5.9). *Chem. Ber.* **1971**, *104*, 1001–1016.
- (26) See Supporting Information.
- (27) Hämäläinen, S. K.; van der Heijden, N.; van der Lit, J.; den Hartog, S.; Liljeroth, P.; Swart, I. Intermolecular Contrast in Atomic Force Microscopy Images without Intermolecular Bonds. *Phys. Rev. Lett.* **2014**, *113*, 186102.
- (28) Hapala, P.; Temirov, R.; Tautz, F. S.; Jelinek, P. Origin of High-Resolution IETS-STM Images of Organic Molecules with Functionalized Tips. *Phys. Rev. Lett.* **2014**, *113*, 226101.
- (29) Hapala, P.; Kichin, G.; Wagner, C.; Tautz, F. S.; Temirov, R.; Jelinek, P. Mechanism of High-Resolution STM/AFM Imaging with Functionalized Tips. *Phys. Rev. B: Condens. Matter Mater. Phys.* **2014**, *90*, 085421.
- (30) Weymouth, A. J.; Hofmann, T.; Giessibl, F. J. Quantifying Molecular Stiffness and Interaction with Lateral Force Microscopy. *Science* **2014**, *343*, 1120–1122.
- (31) van der Lit, J.; Di Cicco, F.; Hapala, P.; Jelinek, P.; Swart, I. Submolecular Resolution Imaging of Molecules by Atomic Force Microscopy: The Influence of the Electrostatic Force. *Phys. Rev. Lett.* **2016**, *116*, 096102.
- (32) Mohn, F.; Gross, L.; Meyer, G. Measuring the Short-Range Force Field above a Single Molecule with Atomic Resolution. *Appl. Phys. Lett.* **2011**, *99*, 053106.

(33) Ishi, S.; Ohno, Y.; Viswanathan, B. An Overview on the Electronic and Vibrational Properties of Adsorbed CO. *Surf. Sci.* **1985**, *161*, 349–372.

(34) Gao, D. Z.; Grenz, J.; Watkins, M. B.; Federici Canova, F.; Schwarz, A.; Wiesendanger, R.; Shluger, A. L. Using Metallic Noncontact Atomic Force Microscope Tips for Imaging Insulators and Polar Molecules: Tip Characterization and Imaging Mechanisms. *ACS Nano* **2014**, *8*, 5339–5351.

(35) Schuler, B.; Liu, W.; Tkatchenko, A.; Moll, N.; Meyer, G.; Mistry, A.; Fox, D.; Gross, L. Adsorption Geometry Determination of Single Molecules by Atomic Force Microscopy. *Phys. Rev. Lett.* **2013**, *111*, 106103.

(36) Bartels, L.; Meyer, G.; Rieder, K. H. Controlled Vertical Manipulation of Single CO Molecules with the Scanning Tunneling Microscope: A Route to Chemical Contrast. *Appl. Phys. Lett.* **1997**, *71*, 213–215.

(37) Albers, B. J.; Schwendemann, T. C.; Baykara, M. Z.; Pilet, N.; Liebmann, M.; Altman, E. I.; Schwarz, U. D. Data Acquisition and Analysis Procedures for High-Resolution Atomic Force Microscopy in Three Dimensions. *Nanotechnology* **2009**, *20*, 264002.

Submolecular Resolution Imaging of Molecules by Atomic Force Microscopy: The Influence of the Electrostatic Force

Joost van der Lit,¹ Francesca Di Cicco,¹ Prokop Hapala,² Pavel Jelinek,² and Ingmar Swart^{1,*}

¹*Debye Institute for Nanomaterials Science, Utrecht University, P.O. Box 80.000, 3508 TA Utrecht, The Netherlands*

²*Institute of Physics, Academy of Sciences of the Czech Republic Cukrovarnicka 10, 1862 53 Prague, Czech Republic*

(Received 10 December 2015; revised manuscript received 19 January 2016; published 3 March 2016)

The forces governing the contrast in submolecular resolution imaging of molecules with atomic force microscopy (AFM) have recently become a topic of intense debate. Here, we show that the electrostatic force is essential to understand the contrast in atomically resolved AFM images of polar molecules. Specifically, we image strongly polarized molecules with negatively and positively charged tips. A contrast inversion is observed above the polar groups. By taking into account the electrostatic forces between tip and molecule, the observed contrast differences can be reproduced using a molecular mechanics model. In addition, we analyze the height dependence of the various force components contributing to the high-resolution AFM contrast.

DOI: [10.1103/PhysRevLett.116.096102](https://doi.org/10.1103/PhysRevLett.116.096102)

The use of frequency modulated atomic force microscopy (FM AFM) as a tool to study molecules has grown tremendously over the past few years. The atomic structure of a single (unknown) molecule can now routinely be identified [1–3]. Even in the case of a complex mixture, the atomic structure of different molecules can be determined [4]. There is increasing interest in extracting quantitative information, such as bond orders, from AFM experiments [5–7].

Several papers have addressed the forces responsible for the submolecular contrast observed in AFM images of molecules [8–13]. It is now well established that the Pauli repulsion, i.e., the increase in the kinetic energy of electrons due to the overlap of electron clouds of the tip and molecule, is one of the most important force components [11]. In addition, van der Waals (vdW) interactions need to be taken into account. Finally, for molecule terminated tips, it is essential to account for the flexibility of the tip [5,8,14]. This flexibility is responsible for image distortions [15] and can enhance the contrast between nonbonded atoms to such an extent that it mimics an apparent bond [8,9,16].

Thus far, mostly pure hydrocarbons were investigated, although recently also some images of molecules containing heteroatoms were published [1,17–20]. In the latter, the charge distribution can be highly nonhomogeneous. For molecules weakly bound to the substrate, the use of chemically passivated tips is essential to avoid accidental pickup of the molecule of interest [2,14]. When molecules are more strongly bound, also more reactive tips can be

used [21,22]. Typically, chemical passivation^{1,*} is achieved by adsorbing a single CO molecule on the tip apex. It is known that a CO molecule adsorbed on a metal has a dipole moment [23,24], the size and direction of which are very sensitive to the adsorption geometry. Hence, when such a charged tip is used to image a polar molecule, it will experience an electrostatic force. Electrostatic forces are known to be important in the imaging of polar substrates [23,25–28]. This raises the question about what the influence of electrostatic forces is in AFM imaging of polar molecules with chemically passivated tips. Here, we investigate how the contrast in AFM images of a molecule with strongly polarized groups (carboxylic acid, triple bond) depends on the charge of the tip. The structure of the molecule bis-(para-benzoic acid) acetylene (BPBA) is shown in Fig. 1(a). The BPBA was deposited on a Au(111) surface, where it forms a self-assembled layer as shown in Fig. 1(b). We acquired high-resolution AFM images with CO and Xe terminated tips, which provide substantially different submolecular contrast. By comparing the experimental data to molecular mechanics simulations, this variation of the submolecular contrast is attributed to a negative (CO) and positive (Xe) charge on the tip [23,29,30]. In particular, we will show that the experimentally observed contrast can only be reproduced in simulations when electrostatic forces are taken into account [29]. Finally, we assess the height dependence of the different force contributions to the contrast.

BPBA molecules (synthesized according to Ref. [31]) were evaporated from a stainless-steel crucible using an e-beam evaporator (Focus GmbH) operated at 0.5 W power onto a clean Au(111) crystal held at 5 K located in a low-temperature STM/AFM (Omicron GmbH). All images were recorded with a qPlus sensor ($f_0 = 21\,922$ Hz, $A_{p-p} = 2$ Å, $Q = 30\,000$). After verification that the

Published by the American Physical Society under the terms of the *Creative Commons Attribution 3.0 License*. Further distribution of this work must maintain attribution to the author(s) and the published article's title, journal citation, and DOI.

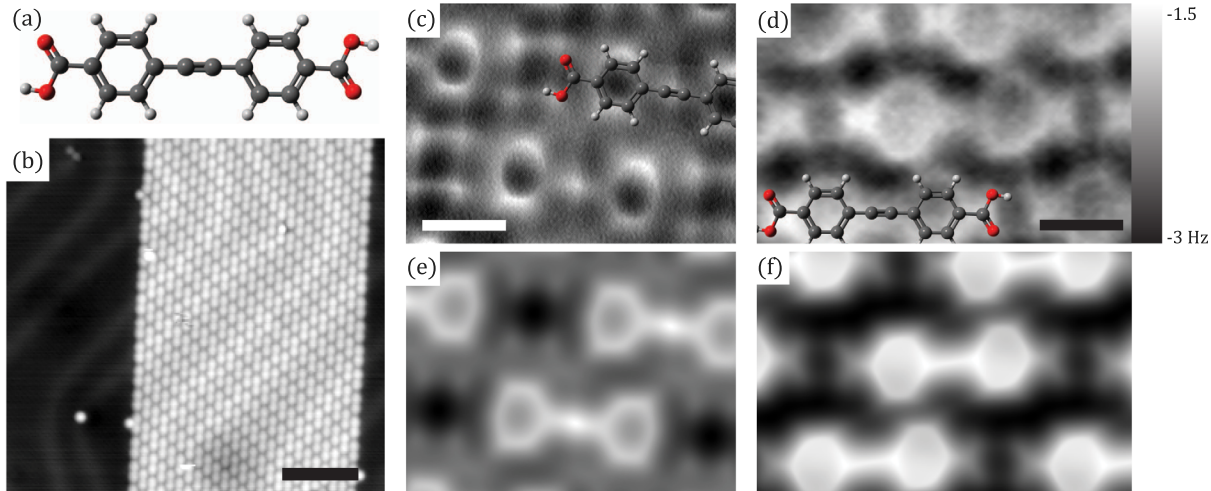


FIG. 1. BPBA molecules on Au(111) imaged with a CO and Xe tip. (a) Model of BPBA. (b) STM image of the self-assembled structure of BPBA on Au(111), 0.1 V, 10 pA, scale bar: 5 nm. (c) Constant height Δf image of BPBA recorded with a CO tip. Image recorded at -1 \AA STM set point (0.1 V, 10 pA), scale bar: 5 \AA . (d) Constant height Δf image of BPBA recorded with a Xe tip. Image recorded at -2.55 \AA STM set point (0.1 V, 10 pA), scale bar: 5 \AA . (e) Simulated Δf image for a CO terminated tip with a $Q_{\text{tip}} = -0.05e^-$ and $k_{x,y} = 0.25 \text{ N/m}$. (f) Simulated Δf image for a Xe tip with a $Q_{\text{tip}} = +0.3e^-$ and $k_{x,y} = 0.25 \text{ N/m}$.

surface coverage was less than a monolayer, the crystal was allowed to heat to 300 K outside the microscope to allow the BPBA to self-assemble into a close-packed structure. The sample was placed back in the microscope after which Xe or CO was dosed onto the cold sample. CO and Xe terminated tips were prepared using standard procedures [32–36]. To minimize the influence of the vdW background, we studied self-assembled structures of BPBA. All AFM images were acquired at 0 V in constant-height mode. The height at which an image was recorded was set with respect to a STM set point (indicated in the text and figure captions). A negative height corresponds to a decrease in the tip-sample distance.

Figure 1(b) shows a STM overview of the self-assembled structure on Au(111). The well-known herringbone reconstruction of the Au(111) surface is clearly visible underneath the patches of molecules. Hence, the BPBA molecules interact weakly with the surface, in agreement with observations made for other molecules on Au(111) [37,38]. Constant-height AFM images acquired with CO and Xe terminated tips are shown in Figs. 1(c) and 1(d). We first discuss the contrast in the images acquired with a CO tip. Both oxygen atoms of the carboxylic acid group are imaged as bright dots. The carboxyl carbon atom (with partial positive charge) is not observed at this tip-sample distance with a CO tip, meaning it is still in the attractive regime. The electron-rich triple bond in the center of the molecule also appears as a bright protrusion when imaged with a CO tip, similar to what has been observed before [3]. Now we discuss how the contrast changes when a Xe terminated tip is used. The carbonyl carbon is imaged as more repulsive than the neighboring oxygen atoms (i.e., less negative frequency shift). In addition, the signature of

the triple bond is no longer clearly resolved. Furthermore, the sizes of various features differ with different tips. Specifically, for these images the apparent distance between the oxygen atoms belonging to the same molecule is smaller with a Xe tip than with the CO tip ($1.6 \pm 0.2 \text{ \AA}$ vs $2.8 \pm 0.2 \text{ \AA}$); i.e., with a Xe tip the carboxylic acid group is imaged as a narrower forklike feature. Finally, the benzene rings appear larger when imaged with a Xe terminated tip (CO, $3.4 \pm 0.1 \text{ \AA}$ vs Xe, $4.4 \pm 0.2 \text{ \AA}$).

To shed light on the relative importance of the various force components, we performed extensive simulations using a periodic molecular mechanics model (AFMulator) [8–10,39], including the electrostatic force [29]. Briefly, the model calculates the tip-sample force (F_{TS}) via pairwise Lennard-Jones (LJ) potentials. Note that these potentials contain terms representing the vdW attraction and Pauli repulsion. In addition, electrostatic forces acting between an effective charge on the tip (Q_{tip}) and electrostatic Hartree potential of the fully relaxed sample [29], as calculated using density-functional theory, are taken into account [40]. The main parameters in the simulations are the lateral force constant and the effective charge of the final atom of the tip denoted as $k_{x,y}$ and Q_{tip} , respectively. The result of the simulations for the Xe and CO tip with $k_{x,y} = 0.25 \text{ N/m}$ and $Q_{\text{tip}} = -0.05e^- / +0.3e^-$ for the CO and Xe terminated tips are shown in Figs. 1(e) and 1(f), respectively. These values for $k_{x,y}$ and Q_{tip} are in agreement with previously reported values [15,29,44]. Our results are robust with respect to small changes in Q_{tip} and $k_{x,y}$ (see the Supplemental Material [40]). All the features observed experimentally (contrast on and size difference in the carboxylic acid group, triple bond, size of benzene rings, discussed above) are reproduced well in the simulations.

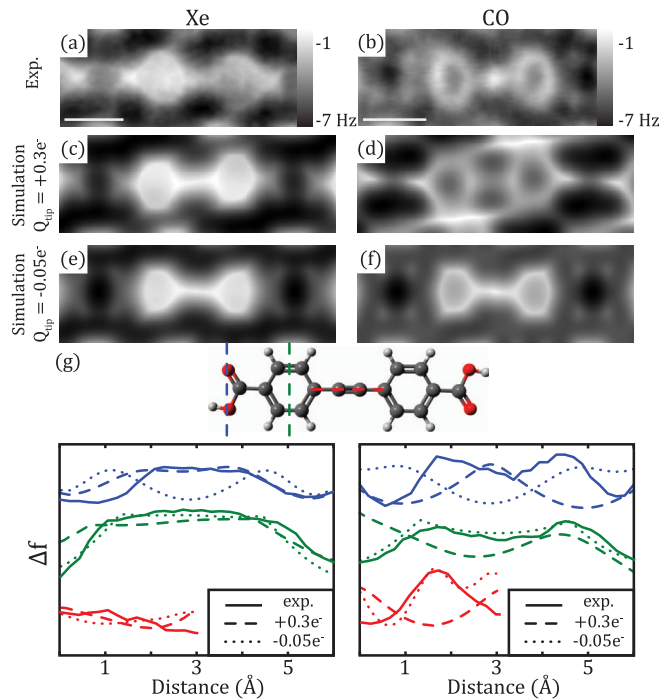


FIG. 2. Importance of tip charge in simulated Δf images of BPBA in self-assembled structures. (a),(b) Constant-height Δf images recorded with Xe and CO tips on a self-assembled layer of BPBA molecules (-3 \AA and -2.4 \AA STM set point $0.1 \text{ V}/10 \text{ pA}$). (c),(d) Simulations with tip charge: $Q_{\text{tip}} = +0.3e^-$ for the Xe and CO terminated tips. (e),(f) Simulations with tip charge $Q_{\text{tip}} = -0.05e^-$ for the Xe and CO terminated tips. $k_{x,y} = 0.25 \text{ N/m}$ in all calculations. (g) Line profiles over characteristic parts of the molecule (indicated in the ball-and-stick model) from experimental data and simulations. Left panel: Xe. Right panel: CO. Scale bars: 5 \AA .

To demonstrate the influence of the electrostatic force, we first calculated two positively charged tips with different LJ potentials: one corresponding to Xe [Fig. 2(c)] and the other one corresponding with CO [Fig. 2(d)] and compared them to experimental images [Figs. 2(a) and 2(b)]. The line profiles from characteristic parts of the molecule are shown in Fig. 2(g). Importantly, the effective positive charge on the CO tip gives a contrast that is comparable to that of the positively charged Xe tip. Namely, we observe a repulsive contrast on the carbonyl carbon and attractive contrast above the oxygen atoms and no clear signature of the triple bond. The additional image features in Fig. 2(d) between the molecules are due to a relatively large partial charge on the tip combined with the small atomic radius of the oxygen atom (1.66 \AA vs 2.18 \AA for O and Xe). The simulation with a negatively charged Xe tip shows similar contrast as the simulation with a negatively charged CO tip, with the exception of the triple bond. These findings conclusively demonstrate that the electrostatic force contribution is essential to understand the contrast in AFM images of polar molecules.

The submolecular contrast is, thus, driven by a combination of the attractive van der Waals forces, the repulsive

Pauli interaction, and the electrostatic interaction that can be both attractive and repulsive. At close distances, the shape of the features, e.g., the apparent position of atoms, strongly depends on the lateral relaxations of the flexible molecule or atom (CO, Xe) attached to the metallic tip apex. This implies that the presence of the electrostatic interaction not only changes the relative intensity of the observed AFM contrast over atoms or bonds, but it also affects the position of sharp contours due to an extra lateral relaxation of the flexible probe. Consequently, both the intensity and the shape of the features in submolecular AFM images acquired with functionalized tips with opposite effective charge (positive Xe and negative CO terminated tips) vary significantly, as shown in Fig. 2. The possibility to use distortions in AFM contrast to extract details about the tip charge and the spatial extent of the electrostatic force will be published elsewhere.

Since the electrostatic force, Pauli repulsion, and vdW attraction have a different distance dependence, it is important to establish the importance of each force component at different heights. To investigate the height dependence of these contributions, we acquired 150 constant-height Δf images with a Xe terminated tip and with a spacing of 5 pm starting from -3.3 \AA with respect to a STM set point of 0.1 V and 10 pA . In addition, we simulated AFM images over the corresponding height range with and without the electrostatic force. Theory and experiment are brought in register by visual identification of the height at which contrast inversion occurs. At close tip-sample distances (-3 \AA), the contrast is determined by the Pauli repulsion [Figs. 3(a)–3(c)]. The bright benzene rings are reproduced in calculations with and without the electrostatic force [Figs. 3(b) and 3(c)]. However, the slight asymmetric position of the benzene rings along the long-molecular axis, as well as the more narrow appearance of the carboxylic acid group is only reproduced in the calculation including the electrostatic force [cf. Figs. 3(a)–3(c)]. At intermediate heights (-2.5 \AA), just after the onset of submolecular resolution, Pauli repulsion over the atoms results in submolecular contrast [Figs. 3(d)–3(f)]. From a comparison between Figs. 3(e) and 3(f), it is clear that the electrostatic force is essential to reproduce the experimentally observed repulsive contrast above the carbonyl carbon. We find that the benzene rings appear larger in simulations with a positively charged tip. Note that in addition to the effective charge of the tip, also the radius of the probe atom and the lateral stiffness of the tip affect the absolute size of the benzene rings. At a tip-sample distance just before the submolecular resolution (-2.1 \AA), the contrast is very dependent on the electrostatic forces [Figs. 3(g)–3(i)]. A calculation with only vdW forces cannot reproduce the experimentally observed contrast above the triple bond (green arrows) and in the area between the molecules (red arrows). At even greater tip-sample separation [-1.3 \AA , Figs. 3(j)–3(l)], the

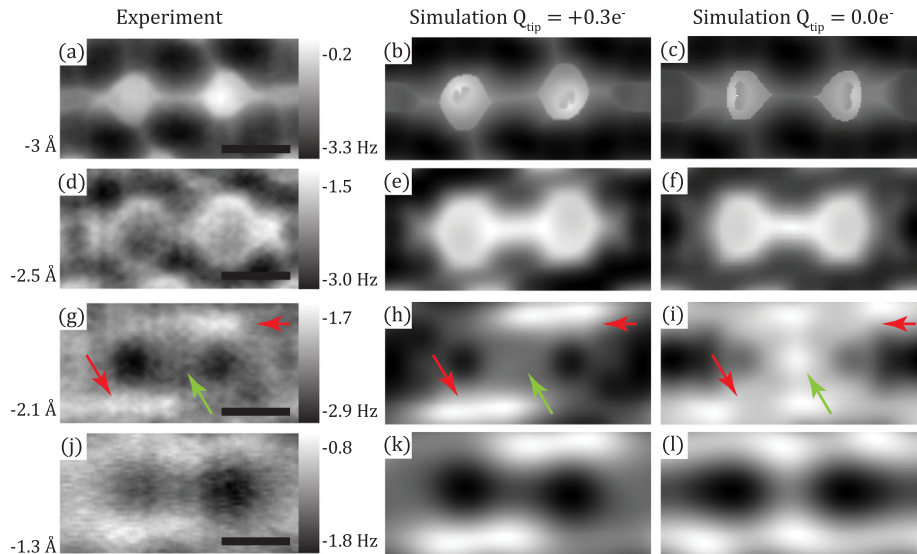


FIG. 3. Height dependence of Δf images with a Xe tip compared to simulations with or without electrostatic force. (a)–(c) Experimental (a) and simulated AFM images with (b) and without (c) electrostatic force ($Q_{\text{tip}} = +0.3e^-$ and $0.0e^-$) at $z = -3 \text{ \AA}$. The tip height was set with respect to a STM set point of 0.1 V and 10 pA. (d)–(f) Same as (a)–(c) but at $z = -2.5 \text{ \AA}$. (g)–(i) same as (a)–(c) but at $z = -2.1 \text{ \AA}$. (j)–(l) Same as (a)–(c) but at $z = -1.3 \text{ \AA}$. Simulations have the same Δz between images as the experiment. All scale bars: 2.5 \AA .

vdW attraction above the benzene rings dominates, and the molecule has a dumbbell shape in simulations with and without electrostatic interactions [Figs. 3(k) and 3(l)]. However, by including electrostatic forces, the agreement with experiment above and immediately next to the triple bond (additional attractive interaction) is improved. We conclude that taking into account electrostatic forces is essential to understand the observed contrast over a wide range of tip-sample distances, even at small distances where the Pauli repulsion dominates. We note here that the model currently does not incorporate the vdW attraction between the molecule and the bulk tip. This additional attractive contribution strongly depends on the macroscopic tip shape, something that is very difficult to control experimentally. However, this long-range vdW component does not generate the submolecular AFM contrast. Because of the relatively flat background in the close-packed self-assembled layer, the omission of the bulk tip will in the present case only result in a rigid offset of the calculated frequency shift values.

In the following, we assess the magnitude of each force contribution as calculated in the molecular mechanics simulations. Figure S2 [40] plots the electrostatic and vdW force-distance components calculated above characteristic molecular sites for both CO and Xe tips. The analysis reveals that the magnitude of the vdW component ($\approx 100 \text{ pN}$) is much larger than the electrostatic counterpart (only a few pN depending on the effective charge on the tip). The magnitude matches previously measured total tip-sample forces on the order of 10–100 pN for CO functionalized tips [2,45]. The sign of the electrostatic component (attractive or repulsive) varies depending on the charge

distribution already at large distances, where the vdW component is mostly monotonically attractive, and the Pauli repulsion is negligible. This further supports the notion that the electrostatic force is essential to understand the contrast in AFM images of molecules at distances where the Pauli repulsion is still negligible.

In conclusion, we imaged strongly polarized BPBA molecules with negatively charged CO and positively charged Xe passivated tips. The combination of experimental high-resolution AFM imaging supported with theoretical modeling unveiled the impact of the electrostatic force acting between the surface and functionalized tip on the resulting submolecular contrast. We observed large differences in the Δf contrast, which can be understood by taking into account the electrostatic contribution to the total force. These differences were observed at all tip-sample distances and contributed significantly to the submolecular AFM contrast. Thus, the electrostatic force plays a very important role in understanding submolecular AFM contrast on strongly polarized molecules.

We thank Peter Spijker and Martin Švec for discussions. This research was supported by the Netherlands Organization for Scientific Research (Chemical Sciences, Veni Grant No. 722.011.007) and the GACR (Project No. 14-16963J).

*I.Swart@uu.nl

[1] L. Gross, F. Mohn, N. Moll, G. Meyer, R. Ebel, W. M. Abdel-Mageed, and M. Jaspars, *Nat. Chem.* **2**, 821 (2010).

- [2] L. Gross, F. Mohn, N. Moll, P. Liljeroth, and G. Meyer, *Science* **325**, 1110 (2009).
- [3] D. G. de Oteyza, P. Gorman, Y.-C. Chen, S. Wickenburg, A. Riss, D. J. Mowbray, G. Etkin, Z. Pedramrazi, H.-Z. Tsai, A. Rubio, M. F. Crommie, and F. R. Fischer, *Science* **340**, 1434 (2013).
- [4] B. Schuler, G. Meyer, D. Peña, O. C. Mullins, and L. Gross, *J. Am. Chem. Soc.* **137**, 9870 (2015).
- [5] L. Gross, F. Mohn, N. Moll, B. Schuler, A. Criado, E. Guitian, D. Pena, A. Gourdon, and G. Meyer, *Science* **337**, 1326 (2012).
- [6] Y. Sugimoto, P. Pou, M. Abe, P. Jelinek, R. Pérez, S. Morita, and O. Custance, *Nature (London)* **446**, 64 (2007).
- [7] M. Ternes, C. P. Lutz, C. F. Hirjibehedin, F. J. Giessibl, and A. J. Heinrich, *Science* **319**, 1066 (2008).
- [8] P. Hapala, G. Kichin, C. Wagner, F. S. Tautz, R. Temirov, and P. Jelínek, *Phys. Rev. B* **90**, 085421 (2014).
- [9] S. K. Hämäläinen, N. van der Heijden, J. van der Lit, S. den Hartog, P. Liljeroth, and I. Swart, *Phys. Rev. Lett.* **113**, 186102 (2014).
- [10] M. P. Boneschanscher, S. K. Hämäläinen, P. Liljeroth, and I. Swart, *ACS Nano* **8**, 3006 (2014).
- [11] N. Moll, L. Gross, F. Mohn, A. Curioni, and G. Meyer, *New J. Phys.* **12**, 125020 (2010).
- [12] J. Zhang, P. Chen, B. Yuan, W. Ji, Z. Cheng, and X. Qiu, *Science* **342**, 611 (2013).
- [13] C.-S. Guo, M. A. Van Hove, X. Ren, and Y. Zhao, *J. Phys. Chem. C* **119**, 1483 (2015).
- [14] H. Mönig, D. R. Hermoso, O. Díaz Arado, M. Todorović, A. Timmer, S. Schüer, G. Langewisch, R. Pérez, and H. Fuchs, *ACS Nano* **10**, 1201 (2016).
- [15] M. Neu, N. Moll, L. Gross, G. Meyer, F. J. Giessibl, and J. Repp, *Phys. Rev. B* **89**, 205407 (2014).
- [16] S. P. Jarvis, M. A. Rashid, A. Sweetman, J. Leaf, S. Taylor, P. Moriarty, and J. Dunn, *Phys. Rev. B* **92**, 241405 (2015).
- [17] S. Kawai, S. Saito, S. Osumi, S. Yamaguchi, A. S. Foster, P. Spijker, and E. Meyer, *Nat. Commun.* **6**, 8098 (2015).
- [18] N. Pavliček, B. Fleury, M. Neu, J. Niefenführ, C. Herranz-Lancho, M. Ruben, and J. Repp, *Phys. Rev. Lett.* **108**, 086101 (2012).
- [19] F. Albrecht, J. Repp, M. Fleischmann, M. Scheer, M. Ondráček, and P. Jelínek, *Phys. Rev. Lett.* **115**, 076101 (2015).
- [20] B. Schuler, S.-X. Liu, Y. Geng, S. Decurtins, G. Meyer, and L. Gross, *Nano Lett.* **14**, 3342 (2014).
- [21] K. Iwata, S. Yamazaki, P. Mutombo, P. Hapala, M. Ondráček, P. Jelínek, and Y. Sugimoto, *Nat. Commun.* **6**, 7766 (2015).
- [22] A. Sweetman, S. P. Jarvis, P. Rahe, N. R. Champness, L. Kantorovich, and P. Moriarty, *Phys. Rev. B* **90**, 165425 (2014).
- [23] M. Schneiderbauer, M. Emmrich, A. J. Weymouth, and F. J. Giessibl, *Phys. Rev. Lett.* **112**, 166102 (2014).
- [24] A. Schwarz, A. Köhler, J. Grenz, and R. Wiesendanger, *Appl. Phys. Lett.* **105**, 011606 (2014).
- [25] F. J. Giessibl, *Phys. Rev. B* **45**, 13815 (1992).
- [26] G. Teobaldi, K. Lämmle, T. Trevethan, M. Watkins, A. Schwarz, R. Wiesendanger, and A. L. Shluger, *Phys. Rev. Lett.* **106**, 216102 (2011).
- [27] F. Bocquet, L. Nony, and C. Loppacher, *Phys. Rev. B* **83**, 035411 (2011).
- [28] R. Hoffmann, D. Weiner, A. Schirmeisen, and A. S. Foster, *Phys. Rev. B* **80**, 115426 (2009).
- [29] P. Hapala, R. Temirov, F. S. Tautz, and P. Jelinek, *Phys. Rev. Lett.* **113**, 226101 (2014).
- [30] L. Gross, B. Schuler, F. Mohn, N. Moll, N. Pavliček, W. Steurer, I. Scivetti, K. Kotsis, M. Persson, and G. Meyer, *Phys. Rev. B* **90**, 155455 (2014).
- [31] H. Dibowski and F. P. Schmidtchen, *Tetrahedron* **51**, 2325 (1995).
- [32] D. M. Eigler, C. P. Lutz, and W. E. Rudge, *Nature (London)* **352**, 600 (1991).
- [33] B. Neu, G. Meyer, and K.-H. Rieder, *Mod. Phys. Lett. B* **09**, 963 (1995).
- [34] A. Yazdani, D. M. Eigler, and N. D. Lang, *Science* **272**, 1921 (1996).
- [35] G. Kichin, C. Weiss, C. Wagner, F. S. Tautz, and R. Temirov, *J. Am. Chem. Soc.* **133**, 16847 (2011).
- [36] L. Bartels, G. Meyer, and K. Rieder, *Appl. Phys. Lett.* **71**, 213 (1997).
- [37] J. van der Lit, M. P. Boneschanscher, D. Vanmaekelbergh, M. Ijäs, A. Uppstu, M. Ervasti, A. Harju, P. Liljeroth, and I. Swart, *Nat. Commun.* **4**, 2023 (2013).
- [38] W.-H. Soe, C. Manzano, A. De Sarkar, N. Chandrasekhar, and C. Joachim, *Phys. Rev. Lett.* **102**, 176102 (2009).
- [39] <https://github.com/ProkopHapala/ProbeParticleModel>.
- [40] See the Supplemental Material at <http://link.aps.org/supplemental/10.1103/PhysRevLett.116.096102>, which includes Refs. [41–43], for a more detailed description of the model, including the parameters used to produce the pair potentials.
- [41] G. Kresse and J. Furthmüller, *Phys. Rev. B* **54**, 11169 (1996).
- [42] J. P. Perdew, J. A. Chevary, S. H. Vosko, K. A. Jackson, M. R. Pederson, D. J. Singh, and C. Fiolhais, *Phys. Rev. B* **46**, 6671 (1992).
- [43] P. E. Blöchl, *Phys. Rev. B* **50**, 17953 (1994).
- [44] A. J. Weymouth, T. Hofmann, and F. J. Giessibl, *Science* **343**, 1120 (2014).
- [45] M. P. Boneschanscher, J. van der Lit, Z. Sun, I. Swart, P. Liljeroth, and D. Vanmaekelbergh, *ACS Nano* **6**, 10216 (2012).

ARTICLE

Received 5 Nov 2015 | Accepted 8 Apr 2016 | Published 27 May 2016

DOI: 10.1038/ncomms11560

OPEN

Mapping the electrostatic force field of single molecules from high-resolution scanning probe images

Prokop Hapala¹, Martin Švec¹, Oleksandr Stetsovych¹, Nadine J. van der Heijden², Martin Ondráček¹, Joost van der Lit², Pingo Mutombo¹, Ingmar Swart² & Pavel Jelínek¹

How electronic charge is distributed over a molecule determines to a large extent its chemical properties. Here, we demonstrate how the electrostatic force field, originating from the inhomogeneous charge distribution in a molecule, can be measured with submolecular resolution. We exploit the fact that distortions typically observed in high-resolution atomic force microscopy images are for a significant part caused by the electrostatic force acting between charges of the tip and the molecule of interest. By finding a geometrical transformation between two high-resolution AFM images acquired with two different tips, the electrostatic force field or potential over individual molecules and self-assemblies thereof can be reconstructed with submolecular resolution.

¹Department of Thin Films and Nanostructures, Institute of Physics, Academy of Sciences of the Czech Republic, v.v.i., Cukrovarnická 10, 162 00 Prague, Czech Republic. ²Department of Chemistry, Condensed Matter and Interfaces, Debye Institute for Nanomaterials Science, Utrecht University, PO Box 80 000, 3508 TA Utrecht, The Netherlands. Correspondence and requests for materials should be addressed to P.J. (email: jelinekp@fzu.cz) or to I.S. (email: i.swart@uu.nl).

Scanning probe techniques routinely provide detailed information on the electronic and geometric structure of molecules. For example, the frontier molecular orbitals¹, the chemical structure of molecules^{2–4} and bond orders⁵ can be imaged. The possibility to image molecules⁶ and atomic clusters⁷ with nearly atomic resolution, also at elevated temperatures^{8–11} provided a great stimulus for surface science^{12–17}.

From the perspective of chemistry, the capability to measure the charge distribution of a molecule is extremely useful as this property determines the chemical reactivity of a molecule, as well as many other molecular properties¹⁸. However, imaging the charge distribution within a single molecule remains a challenge. Thus far, kelvin probe force microscopy (KPFM)¹⁹ is the only technique able to measure a quantity that is related to the charge distribution of an individual molecule²⁰: the local contact potential difference²¹. The acquisition and unambiguous interpretation of KPFM data on the atomic^{22,23} and submolecular level is a non-trivial task^{20,24}. One of the primary difficulties is that there is no clear definition to which physical quantity (electrostatic potential, field or surface dipole and so on) the detected signal should be compared (see, for example, discussion in ref. 25). Furthermore, at the typical tip-sample distances required to obtain submolecular resolution in atomic force microscopy (AFM) images, the measured KPFM signal is governed by the complex interplay of local electrostatic fields of tip and sample, their mutual polarization²⁶, mechanical distortions and the conductance due to overlap of molecular orbitals²⁷. In this regime, the usual interpretation of KPFM data is longer valid²⁸.

Very recently, two alternative techniques, the Scanning Quantum Dot Microscopy²⁹ and the kelvin probe force spectroscopy²⁸, were introduced. Both methods partially solve the deficiencies of the KPFM method discussed above. Namely, Scanning Quantum Dot Microscopy is able to provide a quantitative analysis of the electrostatic potential, but only in the far distance regime, limiting the spatial resolution. The kelvin probe force spectroscopy method provides high spatial resolution but suffers from the same drawback of ambiguous definition of the observable as KPFM (ref. 28).

As the charge distribution is to be imaged with high-resolution resolution, the use of chemically passivated tips is essential^{30–32}. Several different types of forces and processes have been identified to be important for the contrast in AFM images acquired with such tips. These include the Pauli, van der Waals and electrostatic forces, as well as the flexibility of the functionalized tip^{2,5,33–39}. The latter is especially important to understand the distortions in the appearance of molecules in submolecular resolution images^{34,36,40–45}.

Here we will show that the electrostatic forces acting between probe and an inspected molecule can significantly affect the submolecular contrast. Furthermore, we will show that distortions of the high-resolution images induced by the electrostatic force can be used to map the electrostatic potential of the molecule with submolecular resolution.

Results

General considerations. To illustrate the central idea behind the method proposed here, we consider imaging a neutral molecule with an inhomogeneous charge distribution with a tip terminated by a positively charged flexible probe particle. The probe particle is attracted to regions of excess electron density, whereas it is repelled from regions that have a positive charge. Consequently, positively/negatively charged areas will appear smaller/larger than they really are with such a tip, as illustrated in Fig. 1. The opposite tendency is true for negatively charged tips. Hence, the distortions in submolecular resolution AFM images acquired with charged

tips carry information on the charge distribution within the molecule. Here, we demonstrate how these image distortions can be used to determine the spatial distribution of the electrostatic field above molecules with submolecular resolution. The technique is applied to reconstruct the local electrostatic field of both individual molecules and self-assembled monolayers.

First, let us briefly discuss the origin and character of the apparent bonds or sharp edges in high-resolution AFM/STM images. At close tip-sample distances, the repulsive Pauli interaction induces a significant lateral deflection of the probe particle. There is a discontinuity in the deflection above saddle points of the energy landscape (Fig. 2a,b). The saddle points (sharp edges) are typically present over atoms or bonds at a tip-sample distance where the Pauli repulsion fully compensates the attractive forces. Consequently, the trajectory of the probe particle is split into branches, giving rise to sharp edges^{35,38,43}. Hence, the apparent bonds correspond to saddle points of the potential

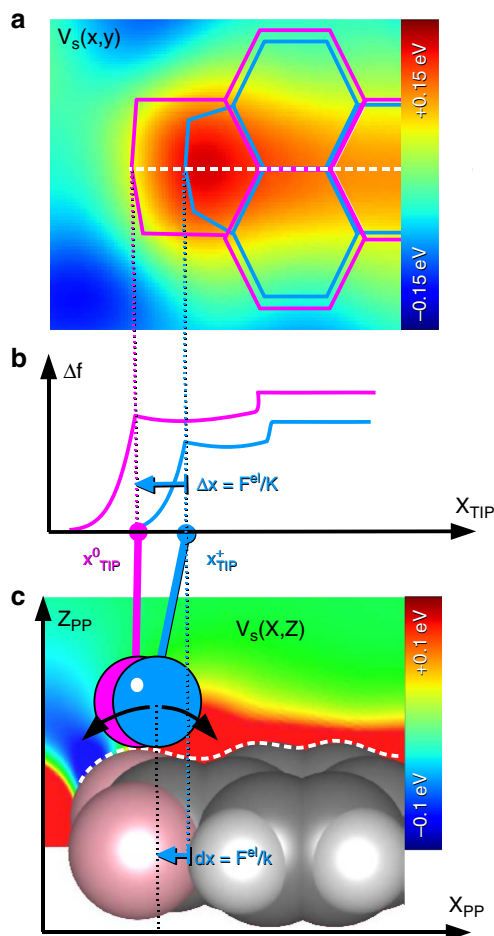


Figure 1 | Schematic view of the impact of the electrostatic forces on the high-resolution AFM images. (a) Blue and pink lines represent the positions of sharp edges observed in high-resolution AFM images acquired using positively charged and neutral tips, respectively. Corresponding x,y cut-plane of the Hartree potential $V_s(x,y)$ above the molecule is displayed in the background. (b) Variation of the frequency shift Δf as function of the tip positions x_{TIP} for the neutral x_{TIP}^0 and positively charged x_{TIP}^+ probe particle. (c) The lateral relaxation Δx of the probe particle with (blue) and without (pink) an effective charge on the tip is different above a molecule due to the presence of the electrostatic force. The electrostatic force originates from the interaction between the electrostatic potential of the molecule (V_s) on the surface and the effective charge on the probe particle at its given position x_{PP} .

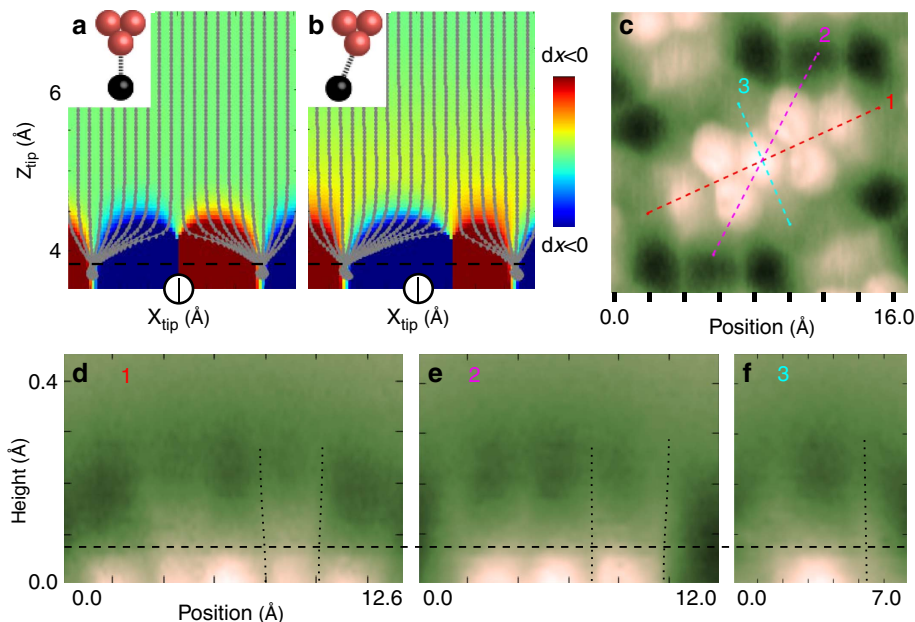


Figure 2 | Height dependence of the position of the sharp edges in AFM images. (a) Simulated deflections of the probe particle as a function of tip position. Grey lines represent the additional deflection of the probe particle with respect to its optimal configuration in far distance. The deflection of the probe particle to the left and right is indicated by blue and red, respectively. (b) Same as **a** but now in the presence of an additional constant lateral force (see Supplementary Fig. 2 and Supplementary Note 2 for more details). (c) Constant-height AFM image of PTCDA on Ag(111). Dashed lines with numbers 1,2,3 denote positions of different vertical cut planes. (d–f) Evolution of Δf with height along the lines shown in **c**. The black dotted lines guide the eye to see relevant edges. The horizontal dashed line indicates the approximate z-distance of contrast inversion.

energy surface experienced by the probe particle at a certain tip-sample distance.

Figure 2a shows the simulated deflections of the probe particle on tip approach over a one-dimensional chain of atoms separated by 2.9 \AA (corresponding to the width of a typical benzene ring). The lateral deflection of the probe particle to the left and right is depicted in blue and red, respectively. Note that the trajectories of the probe particle are split into two branches. The deflection depends non-linearly on the tip height. However, the position of the sharp discontinuous boundary between bending left and right, that is, between blue and red regions, does not depend on the tip-sample distance. This is in agreement with our experimental observation that at close tip-sample distances the apparent position of various sharp edges in AFM images of a perylene-3,4,9,10-tetracarboxylic dianhydride (PTCDA) molecules on Ag(111) does not change with distance (Fig. 2c–f). This finding can be rationalized by the fact that the position of sharp edges is determined by the distance where the bifurcation of the probe particle trajectory on tip approach happens. Consequently, while the lateral distortions of the probe particle may be large beyond this point, the lateral apparent position of the sharp edge remains constant.

The total lateral force F_{tot} is the sum of van der Waals (F_{vdW}), Pauli (F_{Pauli}) and optionally electrostatic (F_{el}) forces. The presence of the lateral force (F_{tot}) induces a lateral deflection (dx) of the flexible probe particle with respect to the tip position (x_{tip}), see Fig. 2b. As long as dx is small, it is linearly proportional to F_{tot} acting on the probe particle, according to Hooke's law: $dx = F_{\text{tot}}/K$ (refs 34,39), where K is the lateral bending stiffness of the bond between the probe particle and the tip. Variation of the lateral electrostatic force F_{el} causes a shift of the characteristic feature at a different lateral tip position (indicated by x_{tip}^+) with respect to the position with the absence of the electrostatic lateral force (x_{tip}^0) as shown in Fig. 1. Consequently, the positions of the apparent bonds (x_{tip}) in high-resolution AFM images do not correspond to their actual positions on the surface.

From the above, it is clear that the apparent shift of the characteristic features (Δx) in AFM/STM images, therefore, carries information about the lateral forces F_{tot} with atomic resolution. The apparent shift is linearly related to the deflection of the probe particle from the tip base: $\Delta x = \gamma dx = \gamma(x_{\text{tip}} - x_{\text{pp}})$, see Fig. 1. Here, x_{pp} denotes the actual position of the probe particle and $\gamma \approx 2$. A detailed quantitative analysis including the definition of the γ coefficient can be found in Supplementary Note 1. In the following discussion, we will express everything in an experimentally observable Δx instead of in dx . In this notation, Δx is linearly proportional to the lateral force: $\Delta x = F_{\text{tot}}/k$, where $k = K/\gamma$ is an effective lateral stiffness.

In our analysis of the electrostatic field, we will use the differences in the apparent positions of sharp contours recorded with two different tips. Specifically, we extract and compare the apparent positions of the same contour feature (for example, a particular atom vertex or bond edge) from two high-resolution AFM images obtained with different tips or scanning conditions (labelled tip A and tip B) at approximately the same tip-sample distances. The apparent position of features acquired with the different tips are indicated by $x_{\text{tip,A}}$ and $x_{\text{tip,B}}$, respectively. In the following, we are interested in the relative difference of the apparent positions $\delta x = x_{\text{tip,A}} - x_{\text{tip,B}}$. Because we measure the same object on the surface, the real position of any atom or bond that corresponds to a particular contour feature is the same for both images. Therefore, δx can be expressed as the difference between the image distortions in the two images of the same object:

$$\delta x = x_{\text{tip,A}} - x_{\text{tip,B}} \quad (1)$$

$$= \Delta x_A - \Delta x_B \quad (2)$$

$$= F_A/k_A - F_B/k_B. \quad (3)$$

Here, F_A and F_B are the total lateral force acting on the probe particle in case A and B, respectively. As shown in the Supplementary Note 1, only the van der Waals and electrostatic

force components of the total force contribute to the apparent lateral distortions $\delta\mathbf{x}$. The reason why $\mathbf{F}_{\text{Pauli}}$ can be ignored is connected with the rather abrupt onset of the Pauli repulsion, as we explain in Supplementary Fig. 1 using our hard-sphere model. The distortion then depends linearly on the lateral van der Waals and electrostatic forces (Supplementary Note 2 and Supplementary Fig. 2). In the following, we therefore use the following expression for the differences in the lateral distortions:

$$\delta\mathbf{x} = \frac{\mathbf{F}_{\text{vdW},A} + \mathbf{F}_{\text{el},A}}{k_A} - \frac{\mathbf{F}_{\text{vdW},B} + \mathbf{F}_{\text{el},B}}{k_B}. \quad (4)$$

In this general form, there is unfortunately no clear way how to attribute partial relative distortions to each force component, for example, to determine the lateral electrostatic force field \mathbf{F}_{el} component only from the high-resolution images. However, under certain assumptions and/or with the help of numerical simulations this problem can be circumvented.

We will now discuss an approach to extract the lateral electrostatic force field component from equation (4). A detailed discussion is given in Supplementary Note 3. In general, the effective stiffness (k) and charge (Q) of the tips, as well as the van der Waals contributions are different for each tip. The charge of the probe particle depends on the configuration and chemical nature of the metal apex⁴⁶, as well as how the Xe/CO is coordinated. Hence, even tips terminated with the same species can have a different charge. First, we will consider the simplest case: two high-resolution images are acquired with (nearly) identical tips, for example, Xe-terminated metallic tips, differing only in their effective charge. In principle, they can have different dipoles instead of effective charges, but this would not change the conclusion drawn later (Supplementary Note 4 and Supplementary Fig. 3). In this case, the following approximations hold: (i) the effective lateral stiffness k of both tips is identical or very similar (that is, $k_A \approx k_B = k$); (ii) the lateral components of the van der Waals forces for tip A and B are also almost identical at a given tip-sample distance. Since both tips are used to image the same object, the surface electrostatic field (\mathbf{E}_S) must be the same in both images. Under these approximations, equation (4) simplifies to:

$$\begin{aligned} \delta\mathbf{x} &= \frac{\mathbf{F}_{\text{el},A} + \mathbf{F}_{\text{el},B}}{k} \\ &= \frac{Q_A - Q_B}{k} \mathbf{E}_S, \end{aligned} \quad (5)$$

where Q_A , Q_B are the effective charges of tips A and B, respectively. This equation shows that we can obtain quantitative information about \mathbf{E}_S directly from the difference in the image distortions. The only parameters that are needed are the effective lateral stiffness k and the difference between the effective charges Q_A and Q_B . These can be estimated for each tip from a direct comparison between experimental and simulated high-resolution AFM/STM images^{35,47} (for more details see Supplementary Method: correlating the experimental and theoretical data sets to obtain the probe characteristics K and Q and Supplementary Fig. 4). Alternatively, k can be obtained directly from experimental measurements⁴⁸.

Next, we consider a more general case where the van der Waals contribution for the two tips is significantly different but one of the tips is neutral, that is, $Q_B \approx 0$. This would correspond to the situation where macroscopically different tips, possibly with different tip termination, are used. In this case, we obtain the following relation for the surface electrostatic field \mathbf{E}_S (for details see Supplementary Note 3):

$$\mathbf{E}_S = \frac{k_A(\delta\mathbf{x} - \delta\mathbf{x}_{\text{vdW}})}{Q_A}, \quad (6)$$

where $\delta\mathbf{x}_{\text{vdW}} = \mathbf{F}_{\text{vdW},A}/k_A - \mathbf{F}_{\text{vdW},B}/k_B$. The differences of the van der Waals deformation field components ($\delta\mathbf{x}_{\text{vdW}}$) can be

estimated from numerical simulations, as discussed later. We note here that the effect of the van der Waals contribution is indispensable only at the periphery of the molecule. Although it may be difficult to extract absolute values in this scenario, the overall shape of the electrostatic field is preserved.

To test our approach to measure the electrostatic field with submolecular resolution, we performed two different sets of experiments. First, we studied a densely packed self-assembled layer of PTCDA on Ag(111) with two differently charged but otherwise similar Xe-terminated tips. Second, we studied individual 1,5,9-trioxo-13-azatriangulene (TOAT) molecules on Cu(111) with a neutral CO terminated tip and a positively charged Xe tip.

Molecular layers of PTCDA on Ag(111). In the case of densely packed self-assembled molecular layers, the van der Waals force component varies slowly. In addition, the effective stiffness k for different tips typically has similar values (see later). Therefore, the term $\delta\mathbf{x}_{\text{vdW}}$ in equation (6) can be neglected and the surface electrostatic field is given by $\delta\mathbf{E}_S = k_A \delta\mathbf{x}/Q_A$.

Figure 3a,b show two constant-height AFM images of a self-assembled monolayer of PTCDA on Ag(111) acquired with a neutral and positively charged Xe tips at the same tip-sample distance (for more details see Methods section). Note that the apparent size of the anhydride groups, indicated by the green circles, is different in the two images. We attribute these differences to a repulsive electrostatic interaction between the positively charged Xe tip and the positively charged anhydride groups⁴⁹. This assignment is supported by a very good agreement between experimental and simulated AFM images of PTCDA/Ag(111) with different effective charges on the Xe tip (Fig. 3c,d). The determined values for k_A , k_B , Q_A and Q_B are: 0.16 Nm^{-1} , 0.20 Nm^{-1} , 0.0 e and $+0.3\text{e}$, respectively, as shown in Supplementary Fig. 4.

The abundant presence of sharp features in the AFM images allows us to use an automatic computer algorithm to determine the differences in the image distortions, that is, $\delta\mathbf{x}$. First, two AFM images are brought into register. Subsequently, the distortion field is found by comparing the corresponding sharp features between the two images. The algorithm is based on matching small regions of the two images. The image is divided into small tiles, in our case regularly distributed circular areas with a diameter of the characteristic image feature (for example, C-C bonds, carbon hexagons and so on). These circular areas are each matched to the other image by moving them laterally, searching for maximum correlation. The resulting shift vectors represent a good approximation of the distortion between the two images, and serve as input for the electrostatic potential determination. The green grids plotted in Fig. 3e,f visualize the determined deformation.

As argued above, the as-obtained deformation field (grey arrows in Fig. 3g) is linearly proportional to the lateral electrostatic field above the molecular layer, with proportionality constant k_A/Q_A . The electrostatic potential obtained from the experimental images is shown in Fig. 3g and is in very good agreement with the electrostatic potential as calculated from density functional theory (DFT; Fig. 3h). The absolute magnitude $+0.04$ to -0.04 eV of the electrostatic field as determined experimentally is approximately three times smaller than estimated from DFT calculations. This discrepancy can be attributed to several effects, such as uncertainties in the absolute tip-sample distance where the electrostatic potential is measured; in the values of the effective charge Q and lateral stiffness k ; in the finite oscillation amplitude and so on. We will address the limits of the method and their possible solutions later (see Discussion).

From the correlation analysis of the experimental and theoretical AFM images of PTCDA (Supplementary Fig. 5), we can estimate the uncertainties in Q and k . For the neutral tip, the maximum correlation is well defined within $\pm 0.05e$ and $\pm 0.08 \text{ Nm}^{-1}$. However, for the positively charged tip there are multiple Q - k combinations that provide a similar correlation between experiment and theory. As the scaling term of the vector field is the ratio Q/k , we can estimate the systematic

error from its variation. By selecting the different favourable Q, k pairs, we find a systematic error of approximately 20%. It is important to note that this uncertainty only affects the absolute values, that is, the relative variation of the electrostatic potential is correct.

Single TOAT molecule on Cu(111). As the second example, we studied individual TOAT molecules, since they have a highly non-homogeneous charge distribution. The central N atom donates an electron to the delocalized π -system and is thus positively charged. In contrast, the three ketone groups at the edge of the molecule withdraw electron density from the ring system and therefore have a partial negative charge. High-pass filtered constant-height AFM images of a TOAT molecule on Cu(111) acquired with CO and Xe tips are shown in Fig. 4a,b, respectively. There are significant differences between images acquired with the two different tip terminations. The central region of the molecule appears smaller while the peripheral benzene rings are elongated for images acquired with a Xe-terminated tip compared to images obtained with a CO tip. Again, this effect is attributed to a repulsive interaction between the positively charged Xe tip and the positively charged central area

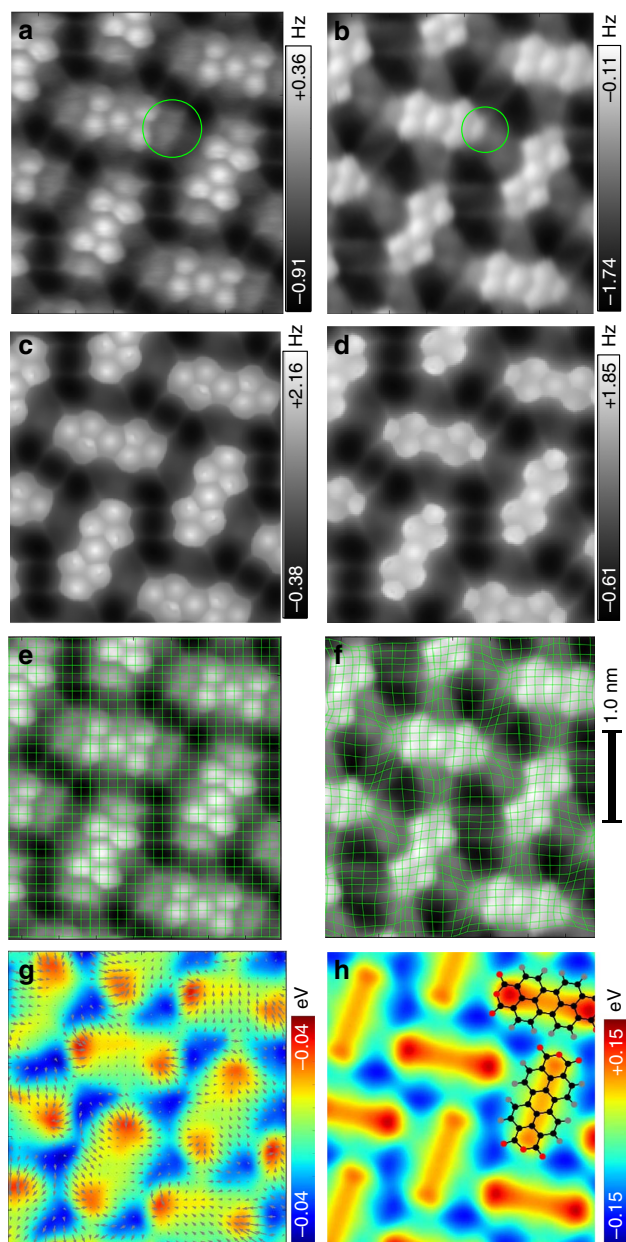


Figure 3 | Determining the electrostatic field above a close-packed PTCDA layer. (a,b) experimental high-resolution AFM images of a self-assembled monolayer of PTCDA deposited on Ag(111) obtained with two different Xe tips. (c) simulated AFM image using an effective charge $Q=0.0e$ and the effective lateral stiffness $k=0.16 \text{ Nm}^{-1}$. (d) same as c but with $Q=+0.3e$ and $k=0.20 \text{ Nm}^{-1}$. (e,f) the experimental images superimposed with a deformation grid defined by comparing the corresponding sharp features between the two images in a and b. (g) electrostatic potential calculated from the deformation field (grey arrows). (h) calculated Hartree potential from DFT simulations 3.0 \AA above the molecular layer.

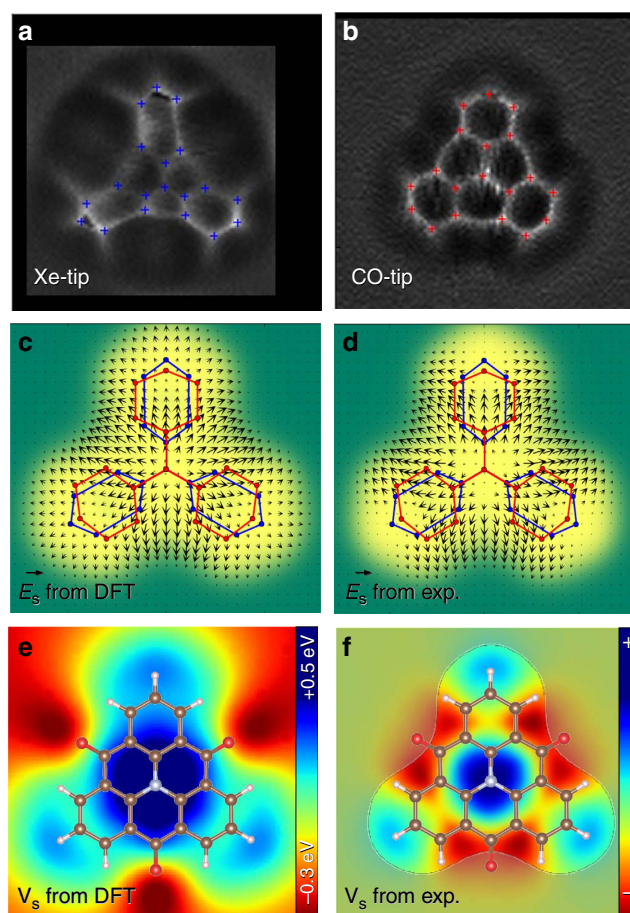


Figure 4 | Determining the electrostatic field above an individual molecule. (a) High-pass filtered constant-height AFM images of a TOAT molecule on Cu(111) acquired with a Xe tip. Crosses indicate characteristic vertices. (b) Same as a but measured with a CO tip. (c) electrostatic force field calculated from DFT. (d) experimentally determined electrostatic force field obtained after subtraction of the van der Waals component from the deformation field obtained from the images shown in a and b. (e) calculated Hartree potential; (f) electrostatic potential calculated from the experimental deformation field shown in d.

of the molecule. This effect is reproduced by our simulations for a Xe tip with an effective charge $Q = +0.3 e$ and lateral stiffness $k = 0.24 \text{ Nm}^{-1}$. Similarly, we found the best match between experimental and theoretical AFM images acquired with the CO tip with an effective charge $Q = 0.0e$ and lateral stiffness $k = 0.24 \text{ Nm}^{-1}$ (details can be found in Supplementary Fig. 5). For individual molecules, positions of vertices were determined manually (blue and red markers in Fig. 4a,b). The deformation field can be obtained by alignment of corresponding vertices ($\delta\mathbf{x}$) in the two AFM images using interpolation by radial basis functions and exploiting the threefold rotational symmetry of the TOAT molecule (see Supplementary Method: estimation of the image distortion from high-resolution AFM images of TOAT molecule and Supplementary Fig. 6). The obtained deformation field shown in Supplementary Fig. 7 is directly proportional to total lateral force field.

Here, the estimated lateral force field also contains the van der Waals force component, which can be determined with the help of numerical modelling³⁴. Thus the electrostatic field E_S can be reconstructed from equation (6) using the fitted lateral stiffness (k_A, k_B) and differential van der Waals deformation field $\delta\mathbf{x}_{\text{vdW}}$ (details of how $\delta\mathbf{x}_{\text{vdW}}$ was subtracted are provided in the Supplementary Method: subtraction of van der Waals component from distortion field on TOAT). Figure 4d shows the as determined electrostatic field while its calculated counterpart is given in Fig. 4c. The agreement between theory and experiment above the molecule is again very good. Note that the method cannot provide resolution outside of the molecule (green area in Fig. 4c,d), due to the lack of sharp features in this region. Hence we nullified the obtained electrostatic field in this area.

For the TOAT molecules, we obtained the experimental electrostatic potential V_S by determining the derivative of the electrostatic field E_S . The resulting electrostatic potential, shown in Fig. 4f, matches the calculated electrostatic field over the molecule including a complex charge distribution on the benzene lobes. The charge distribution near the oxygen atoms can not be described properly due to the lack of sharp features in this area. In the TOAT case, our method cannot reliably quantify the absolute magnitude of the electrostatic potential due to uncertainties associated with subtraction of the vdW force field and the absence of sharp features outside the molecule. We decided not to provide a quantitative comparison of the electrostatic potential V_S to avoid an over-interpretation of our method.

Discussion

We will now discuss several important aspects of the method to facilitate its assessment. The resolution of our method is directly connected to the requirement of having sharp edges in images originating from a saddle point of the potential energy surface. Therefore, the method can only be used to determine the electrostatic field at close tip-sample distances where such features are present.

As discussed above, the position of the sharp edges remains practically constant in the close distance regime. This has two important consequences. First, the position of sharp edges is determined by a bifurcation (cusp) in the probe particle trajectories upon tip approach. The deflection of the probe particle beyond this branching point does not further affect the apparent position of the edges in the images. Consequently, only the value of the lateral spring constant k at the tip-sample distance where the branching occurs will influence the results. Therefore, variations of the lateral stiffness k with tip-sample distance³⁹ do not affect the analysis. Second, our method can only map the electrostatic field at the height where the trajectory of the probe particle branches.

It is important to note that sharp edges are visible in both simultaneously acquired AFM and STM channels, as shown in Supplementary Fig. 8. In addition, sharp features are also present in high-resolution STM (ref. 3) and IETS-STM (ref. 4) images. Hence, in principle, our method can also be applied to such data.

The possibility to extract quantitative information depends critically on several factors. First, uncertainties in the values of k and Q could potentially be eliminated by acquiring two images with the same functionalized tip, the charge of which can be effectively modified by other means (for example, by some oxidation/reduction process of the moiety attached to the tip). A search for new functionalized tips with the possibility to modulate an effective charge without losing its mechanical stability is the subject of current investigations. Alternatively, one can try to reduce the uncertainties in k and Q by, for example, using more sophisticated algorithms for image analysis. The simulation of the electrostatic interaction can be further improved by implementation of a more realistic charge distribution on the probe particle using dipole/quadrupole or even the charge distribution obtained directly from *ab initio* calculations⁵⁰.

In conclusion, we showed that the electrostatic interaction between the probe and a molecule on the surface affects distortions in high-resolution images. In particular, the electrostatic field originating from polar molecules can be mapped with high resolution by analysing the differences in the distortions in images acquired with differently charged tips. The arguments and results presented above demonstrate the background, advantages and limitations of the method to probe the electrostatic potential of molecules with submolecular spatial resolution. The main advantages of this method are the clear relation between the physical observables and the electrostatic field, the high spatial resolution and its applicability to STM and AFM images. In addition, it offers the prospect of extracting quantitative information. Here, we applied the method for molecules, but it can be easily extended to surfaces and surface defects (for example, impurities, vacancies, subsurface defects and so on). As such, it constitutes a valuable complementary tool to existing techniques.

Finally we would like to stress that the general idea behind the technique can be applied to any lateral force acting on the last atom of the tip (the probe particle). Consequently, new potential applications can be envisaged, such as imaging the electrostatic field of the probe itself or that of excited molecules. In addition, it may be possible to map molecular magnetic field as well.

Methods

AFM/STM measurements of PTCDA/Ag(111). The PTCDA on Ag(111) experiments were carried out with a Specs LT STM/AFM with a commercially available Kolibri sensor, operating at $\sim 1.2 \text{ K}$ in ultra-high vacuum. Kolibri sensor parameters used in experiment are: $f_0 \approx 985,387 \text{ Hz}$, $Q \approx 230,000$ and $A \approx 70 \text{ pm}$.

The Ag surface was cleaned by repeated cycles of sputtering (Ar^+ , $p_{\text{Ar}} \approx 5 \times 10^{-6} \text{ mbar}$, 10 min) and annealing ($\approx 800 \text{ K}$, 5 min). PTCDA was evaporated in ultra-high vacuum ($P < 1.5 \times 10^{-9} \text{ mbar}$) for 4 min from a crucible thermally heated to $\approx 673 \text{ K}$. Evaporation was performed $\approx 10 \text{ min}$ after the final annealing of the Ag sample with no post evaporation annealing. Xe (99.99% purity) was deposited on the cold sample ($T < 10 \text{ K}$) by opening shutters for $\approx 14 \text{ s}$ to $p_{\text{Xe}} = 5 \times 10^{-7} \text{ mbar}$. The tip was functionalized in two steps. First, a metal terminated tip was obtained by few nm dipping of the sensor into the clean Ag surface with a $\approx 2 \text{ V}$ bias pulse. Second, Xe-terminated tip was obtained by spontaneous picking up a Xe atom from a Xe island by the metal terminated tip, while scanning in STM mode (0.1 V, 10 pA).

The acquisition of the three-dimensional (3D) force maps was done automatically, by measuring a sequence of constant-height images and changing the tip-sample separation in between the subsequent images. Apart from the frequency shift, tunnelling current, dissipation and also the amplitude channels have been recorded simultaneously. The step in z was chosen to be in the order of picometres and positive, that is, increasing the tip-sample distance.

Images acquired with different tips were aligned vertically using the following procedure. First, for each tip a data cube with simulated 3D frequency shift values is generated for a particular set of k and Q values. The offsets in z -distance of the

experimental and theoretical data sets are then determined by aligning the z -position of the frequency shift minimum for the centres of the molecules. Once this information is available for each tip, images corresponding to approximately the same tip-sample distance can be selected.

AFM/STM measurements of TOAT/Cu(111). Individual TOAT molecules on Cu(111) with a neutral CO terminated tip and a positively charged Xe tip were imaged using a Scienta-Omicron LT STM/AFM with a commercially available Qplus sensor, operating at ~ 4.6 K in ultrahigh vacuum with an average pressure of 5×10^{-10} mbar. The baked qPlus sensor (3 h at 120 °C) had a quality factor of $Q = 30,000$, a resonance frequency of $f_0 = 25,634$ Hz and a peak-to-peak oscillation amplitude of approximately 2 Å.

A Cu(111) crystal surface was cleaned with several sputter and anneal cycles before inserting it in the microscope head. The TOAT molecules were thermally evaporated onto the cold surface using an e-beam evaporator (Focus GmbH). For STM imaging, the bias voltage was applied to the sample. After approaching the tip to the surface, an atomically sharp metal tip was prepared by controlled crashes into the copper surface and bias pulses. Each chemically passivated tip was prepared by subsequent pick-up of either a Xe atom or CO molecule^{2,51–53}. After a free-lying TOAT molecule was located on the surface, the tip was left in tunnelling contact ($I = 10$ pA at $V = 0.1$ V) and allowed to relax for 12 h to minimize drift and piezo-creep. All AFM images were acquired in constant-height mode. After each AFM image, the STM feedback loop was enabled for 2 s to further minimize tip-sample drift. A complete stack of images resulting in a 3D force grid took ~ 13 h to acquire.

DFT calculation of PTCDA/Ag(111). We used a pre-optimized herringbone structure of PTCDA molecules on Ag(111) surface⁵⁴ consisting of two molecules in the unit cell and a slab of 3 Ag layers (99 Ag atoms). The Hartree potential used for generating the theoretical electrostatic field⁵⁵ was obtained from self-consistent total energy DFT using the Vienna ab initio simulation package⁵⁵ with generalized gradient approximation based functional PW91 (ref. 56) and projector augmented-wave method⁵⁷. Plane wave basis set was chosen with $E_{\text{cut}} = 396$ eV.

DFT calculation of TOAT/Cu(111). Total energy DFT calculations were performed using the FHI-aims code⁵⁸. We used a 6×6 supercell made of four Cu layers to describe the Cu(111) surface. The TOAT molecule was placed on the surface with the N atom in a top position. This position was chosen based on the experimental findings. All the atoms except the two bottom Cu layers were relaxed until the remaining atomic forces and the total energy were below 10^{-2} eV Å⁻¹ and 10^{-5} eV, respectively. A Monkhorst-Pack grid of $2 \times 2 \times 1$ was used for the integration in the Brillouin zone. All the calculations were carried out at the GGA-PBE level⁵⁹ including the Tkatchenko-Scheffler treatment⁶⁰ of the van der Waals interaction. The use of van der Waals interactions was necessary to correctly describe the interaction between the molecule and surface. The basis set, pseudo-potentials, integration grids and Hartree potential accuracy were specified using the 'tight' settings. For species like H, O, N the basis set level was set to 'tier 2' while for Cu a first tier was used. Note that a 'tier' represents a single set of radial functions added to the minimal basis to effectively describe the chemical bond.

AFM simulations. To calculate high-resolution AFM images we used a home built AFM simulation toolkit^{34,35} (available opensource at <https://github.com/ProkopHapala/ProbeParticleModel>; see also webpage <http://nanosurf.fzu.cz/ppr/>). We used default parameters of pairwise LJ potentials³⁴. The optimized structures and corresponding surface Hartree potentials were obtained from fully relaxed total energy DFT simulations of the system, see above. The effective tip charge Q and lateral stiffness k of probe particle are a free input of the model. The positions of the $Af(z)$ minima in the centres of the molecules were taken as the reference points in Z , for both the experiment and theory.

Processing of experimental data and matching to simulation. Iterative algorithm for registration of experimental AFM/STM images using linear correlation is described in the Supplementary Method: data set registration procedure and Supplementary Fig. 9. The estimation of the effective stiffness K and effective charge Q is described in the Supplementary Method: correlating the experimental and theoretical data sets to obtain the probe characteristics K and Q and Supplementary Fig. 4 for PTCDA and Supplementary Fig. 5 for TOAT. The evaluation of the electrostatic potential by fitting its derivatives to image distortions is described in the Supplementary Method: evaluation of the electrostatic potential from the distortion vector field.

Data availability. The data that support the findings of this study are available from the corresponding authors on request.

References

- Repp, J., Meyer, G., Stojkovic, S. M., Gourdon, A. & Joachim, C. Molecules on insulating films: scanning-tunneling microscopy imaging of individual molecular orbitals. *Phys. Rev. Lett.* **94**, 026803 (2005).
- Gross, L., Mohn, F., Moll, N., Liljeroth, P. & Meyer, G. The chemical structure of a molecule resolved by atomic force microscopy. *Science* **325**, 1110–1114 (2009).
- Temirov, R., Soubatch, S., Neucheva, O., Lassise, A. C. & Tautz, F. S. A novel method achieving ultra-high geometrical resolution in scanning tunnelling microscopy. *New J. Phys.* **10**, 053012 (2008).
- Chiang, C. L., Xu, C., Han, Z. & Ho, W. Real-space imaging of molecular structure and chemical bonding by single-molecule inelastic tunneling probe. *Science* **344**, 885–888 (2014).
- Gross, L. *et al.* Bond-order discrimination by atomic force microscopy. *Science* **337**, 1326–1329 (2012).
- Gross, L. Recent advances in submolecular resolution with scanning probe microscopy. *Nat. Chem.* **3**, 273–278 (2011).
- Emmrich, M. *et al.* Subatomic resolution force microscopy reveals internal structure and adsorption sites of small iron clusters. *Science* **348**, 308–311 (2015).
- Sweetman, A. *et al.* Intramolecular bonds resolved on a semiconductor surface. *Phys. Rev. B* **90**, 165425 (2014).
- Iwata, K. *et al.* Chemical structure imaging of a single molecule by atomic force microscopy at room temperature. *Nat. Commun.* **6**, 7766 (2015).
- Moreno, C., Stetsovych, O., Shimizu, T. K. & Custance, O. Imaging three-dimensional surface objects with submolecular resolution by atomic force microscopy. *Nano Lett.* **15**, 2257–2262 (2015).
- Huber, F. *et al.* Intramolecular force contrast and dynamic current-distance measurements at room temperature. *Phys. Rev. Lett.* **115**, 066101 (2015).
- de Oteyza, D. G. *et al.* Direct imaging of covalent bond structure in single-molecule chemical reactions. *Science* **340**, 1434–1437 (2013).
- Pavlicek, N. *et al.* Atomic force microscopy reveals bistable configurations of dibenzo[a,h]thianthrene and their interconversion pathway. *Phys. Rev. Lett.* **108**, 08610 (2012).
- Kawai, S. *et al.* Obtaining detailed structural information about supramolecular systems on surfaces by combining high-resolution force microscopy with ab initio calculations. *ACS Nano* **7**, 9098–9105 (2013).
- Schuler, B., Meyer, G., Peña, D., Mullins, O. C. & Gross, L. Unraveling the molecular structures of asphaltenes by atomic force microscopy. *J. Am. Chem. Soc.* **137**, 9870–9876 (2015).
- Pavlicek, N. *et al.* On-surface generation and imaging of arynes by atomic force microscopy. *Nat. Chem.* **7**, 623–628 (2015).
- Dienel, T. *et al.* Resolving atomic connectivity in graphene nanostructure junctions. *Nano Lett.* **15**, 5185–5190 (2015).
- Clayden, J., Greeves, N. & Warren, S. *Organic Chemistry* (Oxford University Press, 2001).
- Nonnenmacher, M., O'Boyle, M. P. & Wickramasinghe, H. K. Kelvin probe force microscopy. *Appl. Phys. Lett.* **58**, 2921 (1991).
- Mohn, F., Gross, L., Moll, N. & Meyer, G. Imaging the charge distribution within a single molecule. *Nat. Nanotechnol.* **7**, 227–231 (2012).
- Baier, R., Leendertz, C., Lux-Steiner, M. C. & Sadewasser, S. Toward quantitative Kelvin probe force microscopy of nanoscale potential distributions. *Phys. Rev. B* **85**, 165436 (2012).
- Enevoldsen, G. H., Glatzel, T., Christensen, M. C., Lauritsen, J. V. & Besenbacher, F. Atomic scale kelvin probe force microscopy studies of the surface potential variations on the TiO₂(110) surface. *Phys. Rev. Lett.* **100**, 236104 (2008).
- Sadewasser, S. *et al.* New insights on atomic-resolution frequency-modulation kelvin-probe force-microscopy imaging of semiconductors. *Phys. Rev. Lett.* **103**, 266103 (2009).
- Schuler, B. *et al.* Contrast formation in Kelvin probe force microscopy of single π -conjugated molecules. *Nano Lett.* **14**, 3342–3346 (2014).
- Neff, J. L. & Rahe, P. Insights into Kelvin probe force microscopy data of insulator-supported molecules. *Phys. Rev. B* **91**, 085424 (2015).
- Corso, M. *et al.* Charge redistribution and transport in molecular contacts. *Phys. Rev. Lett.* **115**, 136101 (2015).
- Weymouth, A., Wutscher, T., Welker, J., Hofmann, T. & Giessibl, F. Phantom force induced by tunneling current: a characterization on Si(111). *Phys. Rev. Lett.* **106**, 226801 (2011).
- Albrecht, F. *et al.* Probing charges on the atomic scale by means of atomic force microscopy. *Phys. Rev. Lett.* **115**, 076101 (2015).
- Wagner, C. *et al.* Scanning quantum dot microscopy. *Phys. Rev. Lett.* **115**, 026101 (2015).
- Bartels, L. *et al.* Dynamics of electron-induced manipulation of individual CO molecules on Cu(111). *Phys. Rev. Lett.* **80**, 2004 (1998).
- Welker, J. & Giessibl, F. J. Revealing the angular symmetry of chemical bonds by atomic force microscopy. *Science* **336**, 444–449 (2012).
- Mohn, F., Schuler, B., Gross, L. & Meyer, G. Different tips for high-resolution atomic force microscopy and scanning tunneling microscopy of single molecules. *Appl. Phys. Lett.* **102**, 073109 (2013).

33. Moll, N., Gross, L., Mohn, F., Curioni, A. & Meyer, G. The mechanisms underlying the enhanced resolution of atomic force microscopy with functionalized tips. *New J. Phys.* **12**, 125020 (2010).
34. Hapala, P. *et al.* The mechanism of high-resolution STM/AFM imaging with functionalized tips. *Phys. Rev. B* **90**, 085421 (2014).
35. Hapala, P., Temirov, R., Tautz, F. S. & Jelinek, P. Origin of high-resolution IETS-STM images of organic molecules with functionalized tips. *Phys. Rev. Lett.* **113**, 226101 (2014).
36. Guo, C., Xin, X., Van Hove, M. A., Ren, X. & Zhao, Y. Origin of the contrast interpreted as intermolecular and intramolecular bonds in atomic force microscopy images. *J. Phys. Chem. C* **119**, 14195–14200 (2015).
37. van der Lit, J., Di Cicco, F., Hapala, P., Jelinek, P. & Swart, I. Submolecular resolution imaging of molecules by atomic force microscopy: the influence of the electrostatic force. *Phys. Rev. Lett.* **105**, 096102 (2016).
38. Boneschanscher, M. P., Hämäläinen, S. K., Liljeroth, P. & Swart, I. Sample corrugation affects the apparent bond lengths in atomic force microscopy. *ACS Nano* **8**, 3006–3014 (2014).
39. Neu, M. *et al.* Image correction for atomic force microscopy images with functionalized tips. *Phys. Rev. B* **89**, 205407 (2014).
40. Zhang, J. *et al.* Real-space identification of intermolecular bonding with atomic force microscopy. *Science* **342**, 611–614 (2013).
41. Sweetman, A. M. *et al.* Mapping the force field of a hydrogen-bonded assembly. *Nat. Commun.* **5**, 3931 (2014).
42. Moll, N. *et al.* Image distortions of a partially fluorinated hydrocarbon molecule in atomic force microscopy with carbon monoxide terminated tips. *Nano Lett.* **14**, 6127–6131 (2014).
43. Hämäläinen, S. K. *et al.* Intermolecular contrast in atomic force microscopy images without intermolecular bonds. *Phys. Rev. Lett.* **113**, 186102 (2014).
44. Kawai, S. *et al.* Extended halogen bonding between fully fluorinated aromatic molecules. *ACS Nano* **9**, 2574–2583 (2015).
45. Jarvis, S. P. *et al.* Intermolecular artifacts in probe microscope images of C60 assemblies. *Phys. Rev. B* **92**, 241405 (2015).
46. Gao, D. Z. *et al.* Using metallic noncontact atomic force microscope tips for imaging insulators and polar molecules: tip characterization and imaging mechanisms. *ACS Nano* **8**, 5339–5351 (2014).
47. Sun, Z., Boneschanscher, M., Swart, I., Vanmaekelbergh, D. & Liljeroth, P. Quantitative atomic force microscopy with carbon monoxide terminated tips. *Phys. Rev. Lett.* **106**, 046104 (2011).
48. Weymouth, A. J., Hofmann, T. & Giessibl, F. J. Quantifying molecular stiffness and interaction with lateral force microscopy. *Science* **343**, 1120–1122 (2014).
49. Gross, L. *et al.* Investigating atomic contrast in atomic force microscopy and Kelvin probe force microscopy on ionic systems using functionalized tips. *Phys. Rev. B* **90**, 155455 (2014).
50. Ellner, M. *et al.* The electric field of CO tips and its relevance for atomic force microscopy. *Nano Lett.* **16**, 1974–1980 (2016).
51. Eigler, D. M., Lutz, C. P. & Rudge, W. E. An atomic switch realized with the scanning tunnelling microscope. *Nature* **352**, 600–603 (1991).
52. Bartels, L., Meyer, G. & Rieder, K.-H. Controlled vertical manipulation of single CO molecules with the scanning tunneling microscope: a route to chemical contrast. *Appl. Phys. Lett.* **71**, 213–215 (1997).
53. Giessibl, F. Advances in atomic force microscopy. *Rev. Mod. Phys.* **75**, 949 (2003).
54. Rohlfing, M., Temirov, R. & Tautz, F. Adsorption structure and scanning tunneling data of a prototype organic-inorganic interface: PTCDA on Ag(111). *Phys. Rev. B* **76**, 115421 (2007).
55. Kresse, G. & Furthmüller, J. Efficient iterative schemes for ab initio total-energy calculations using a plane-wave basis set. *Phys. Rev. B* **54**, 11169 (1996).
56. Perdew, J. P. *et al.* Atoms, molecules, solids, and surfaces: applications of the generalized gradient approximation for exchange and correlation. *Phys. Rev. B* **46**, 6671–6687 (1992).
57. Kresse, G. & Joubert, D. From ultrasoft pseudopotentials to the projector augmented-wave method. *Phys. Rev. B* **59**, 1758–1775 (1999).
58. Blum, V. *et al.* Ab initio molecular simulations with numeric atom-centered orbitals. *Comput. Phys. Commun.* **180**, 2175–2196 (2009).
59. Perdew, J. P., Burke, K. & Ernzerhof, M. Generalized gradient approximation made simple. *Phys. Rev. Lett.* **77**, 3865–3868 (1996).
60. Tkatchenko, A. & Scheffler, M. Accurate molecular van der waals interactions from ground-state electron density and free-atom reference data. *Phys. Rev. Lett.* **102**, 073005 (2009).

Acknowledgements

This work was financially supported by grants from the Czech Science Foundation (grant no. 14-16963J), the Ministry of Education of the Czech Republic grant no. LM2015087 and the Netherlands Organization for Scientific Research (ECHO-STIP grant no. 717.013.003).

Author contributions

P.H., M.Š. and P.J. conceived the method. I.S. and P.J. conceived the experiments. M.Š., O.S., J.L., N.J.v.d.H. and I.S. carried out the experiments and analysed the experimental data. P.H., M.O., P.M. and P.J. performed and analysed the total energy DFT and AFM calculations. P.H., I.S., M.Š. and P.J. wrote the paper. All coauthors provided feedback on the manuscript.

Additional information

Supplementary Information accompanies this paper at <http://www.nature.com/naturecommunications>

Competing financial interests: The authors declare no competing financial interests.

Reprints and permission information is available online at <http://npj.nature.com/reprintsandpermissions/>

How to cite this article: Hapala, P. *et al.* Mapping the electrostatic force field of single molecules from high-resolution scanning probe images. *Nat. Commun.* **7**:11560 doi: 10.1038/ncomms11560 (2016).



This work is licensed under a Creative Commons Attribution 4.0 International License. The images or other third party material in this article are included in the article's Creative Commons license, unless indicated otherwise in the credit line; if the material is not included under the Creative Commons license, users will need to obtain permission from the license holder to reproduce the material. To view a copy of this license, visit <http://creativecommons.org/licenses/by/4.0/>